The Effect of Energy Input on Precipitation in an Oscillating Grid Reactor.

A Thesis submitted for the Degree of

Master of Science

By:

Botlhe Tshimologo Mokgethi

B.Sc Chemical Engineering (University of Cape Town**)**

Faculty of Engineering and Built Environment

University of Cape Town

2010

I hereby certify that the work embodied in this thesis is the result of original research and has not been submitted for another degree at any university or institution.

_____

Botlhe Tshimologo Mokgethi
2010

Dedication

To my mother and father for their patience, understanding, encouragement and loving support throughout this project.

Acknowledgments

I would like to acknowledge the following people, without whom this project would not be possible:

- Appreciation is expressed to my supervisors, Associate Professor David A. Deglon and Professor Alison E. Lewis for their sustained interest and guidance in carrying out this research project and in the preparation of this thesis.

- Helen Divey and the laboratory staff of the Department of Chemical Engineering for their help with the chemical analyses.

- Many thanks to Melinda Waldron of the Electron Microscope Unit (EMU) at UCT for her assistance in using the SEM.

- The staff and students of the Minerals to Metals students and Crystallization and precipitation research unit for their valuable assistant, comments and constructive advice.

- Finally appreciation is expressed to the Minerals to Metals initiative staff for the funding of this project and to Professor J-P Franzidis for his continuous encouragement.

Synopsis

The move to cleaner production has led to the process industry aiming at producing chemicals in a pure form and at the lowest possible cost. In practice this has resulted in a shift from treating processes as “black boxes” towards developing more concise models which reveal what happens within these “black boxes”. This shift can be discerned at plant level for better control mechanisms, at a reactor design level to incorporate the effect of hydrodynamics and even at a molecular level when designing a tailor-made catalyst.

The conventional reactor system used in precipitation processes is the stirred tank. Although the hydrodynamic environments in stirred tanks are well defined, the turbulence in these vessels is inhomogeneous and anisotropic. These complex environments mean that modelling and quantifying the effect of hydrodynamics on precipitation is challenging. This is because the models used in precipitation processes are based on the assumption of homogeneous isotropic turbulence. Oscillating grids exhibit near isotropic and homogeneous turbulence, which cannot be achieved in impeller agitated tanks. This is the simplest form of turbulence and it has the minimum number of quantities and relations required to describe it. Investigating and characterising precipitation kinetics in such environments can provide an essential building block to the understanding of what occurs in more complex flow systems that are experienced on an industrial scale.

In view of the above problem, the objective of the present study is to gain an understanding of the precipitation kinetics (in particular aggregation) in a nearly homogeneous isotropic turbulent environment through investigating the effect energy input on the precipitation of calcium oxalate monohydrate (COM). To achieve the set objective, experiments were carried out in an oscillating multi-grid reactor run in batch mode. The reactor consists of a 10 litre tank agitated by 19 grids which have a mesh size of 8mm and a grid spacing of 18 mm. The effect of energy input on aggregation was investigated by studying the X-ray diffraction (XRD) patterns of the precipitate formed,

the scanning electron microscopy (SEM) micrographs of the precipitate, the volume or mass equivalent mean ($D_{4,3}$), the number based mean ($L_{1,0}$) and the aggregation kernel (β_0).

The SEM results show that the crystals precipitate out in the typical monoclinic prismatic shape appearing as flat elongated jagged platelets. At low energy inputs, the crystals have a more defined crystallographic axis as compared to crystals produced at high energy inputs. This indicates that at low energy inputs growth is a more dominant process whereas aggregation becomes more apparent at higher energy inputs.

The trend for the number based mean shows that at low energy inputs ($0 < \varepsilon < 0.1$ W/kg), there is a decrease in the $L_{1,0}$. At higher energy inputs ($\varepsilon > 0.1$ W/kg), $L_{1,0}$ increases with increasing energy input. This decrease in $L_{1,0}$ indicates the increase in the presence of smaller particles which is due to nucleation whereas the increase in the $L_{1,0}$ is due to aggregation. The trend for the weight equivalent mean increases as energy input increases ($0 < \varepsilon < 0.1$ W/kg), reaching a maximum and then decreases. This increase in the $D_{4,3}$ could be due to aggregation and (or) growth. The decrease in the mean size at higher energy inputs is due to breakage and a decrease in aggregation efficiency.

A maximum is exhibited in the size independent aggregation kernel at 0.049 W/kg, suggesting a decrease in aggregation efficiency and breakage at higher energy inputs. This trend shows the disruptive role of hydrodynamics on aggregation at high shears.

Table of contents

List of figures

List of tables

Nomenclature

A: crystal surface area (m^2)

B: birth rate ($m^{-1}.m^3.s^{-1}$)

B^0: nucleation rate ($\#.s^{-1}s.m^{-3}$)

C_1, C_2: tank-geometry dependant constants

c*: saturation concentration ($kmol.m^{-3}$)

C^*: concentration at the crystal surface ($mol.m^{-3}$)

C_i: solute concentration at the solid-liquid interface ($mol.m^{-3}$)

C_{eq}: solubility of the precipitating species ($mol.m^{-3}$)

C_i: solute concentration at the solid-liquid interface ($mol.m^{-3}$)

C_b: bulk solute concentration ($mol.m^{-3}$)

c: actual concentration($kmol.m^{-3}$)

$[Ca^{2+}]$: concentration of calcium in solution ($mg.L^{-1}$)

D: diameter of impeller (m)

D_{meso}: turbulent diffusivity ($m.s^{-1}$)

E: energy spectrum function ($m^2.s^{-1}$)

$F_{n,g}$: net applied force to the liquid by the grid ($kg.m.s^{-2}$)

F_f: gross force in the column filled with the liquid ($kg.m.s^{-2}$)

F_i: net force in the column when empty ($kg.m.s^{-2}$)

f: grid vibrating frequency (s^{-1})

k: Boltzmann constant ($m^2.kg.s^{-2}.K^{-1}$)

k_d: mass transfer coefficient ($m.s^{-1}$)

k_i: surface reaction rate constant ($kmol^{1-m}.m^{3m-2}.s^{-1}$)

$L_{i,}$ L_j : size of particles (m)

$L_{1,0}$: number based mean size (m)

M: grid mesh size (cm)

m_l : mass of liquid in column (kg)

m: order of the surface reaction (-)

m_0: total number of particles per unit crystallizer volume ($\#.m^{-3}$)

m_1: total length of particles per unit crystallizer volume ($m.m^{-3}$)

m_2: related to the total surface area of particles per crystallizer volume ($m^2.m^{-3}$)

m_3: related to the total volume of particles per crystallizer volume ($m^3.m^{-3}$)

n: frequency (s^{-1})

N: impeller speed (s^{-1})

N_q: flow number (-)

N: impeller speed (s^{-1})

N_p: power number (-)

P: power dissipation (W)

P_g: power input to the grid, power lost due to skin friction ($N.m.s^{-1}$)

Q: volumetric flow rate ($m^2.s^{-1}$)

r: radial coordinate (m)

R: internal radius of tube (m)

S: grid stroke (cm)

S: supersaturation ratio (-)

T: temperature (K)

$t_{r,}$ t_{rmin}: residence time, minimum residence time (s)

u(t): turbulent fluctuation component ($m.s^{-1}$)

u , u_{max}: velocity, maximum velocity ($m.s^{-1}$)

v(t): turbulent velocity ($m.s^{-1}$)

$\bar{v}$: mean velocity ($m.s^{-1}$)

V: vessel volume (m^3)

V_L: volume of liquid in vessel (m^3)

z: vertical distance (cm)

Greek Letters

ε: energy dissipation rate ($W.kg^{-1}$)

ρ_L: density of liquid ($kg.m^{-3}$)

γ, γ_{max}: shear rate, maximum shear rate (s^{-1})

σ: relative supersaturation (-)

σ: surface tension ($dynes.cm^{-1}$)

ν: fluid kinematic viscosity (m^2s^{-1})

$\hat{v}$: instantaneous velocity ($m.s^{-1}$)

υ: molecular volume ($cm^3.g^{-1}$)

Chapter 1. Introduction

1.1. Overview

The understanding of mixing processes which occur in stirred tanks is an important aspect for the design of many industrial processes such as precipitation, flotation and biochemical processes. Smith (1990) reported that the lack of a fundamental understanding of the processes in stirred vessels leads to losses of the order of US$10 billion per year due to non-optimal energy utilization. The economics of a process depend on the performance of a stirred tank with respect to mixing, power consumption, the rate of reactions as well as the product quality. Mixing in stirred tanks is driven by the impeller generated convective motion at larger scales, by turbulent transfer at smaller scales and down to diffusion at molecular scales (Nagata, 1975).

Crystallization is a separation and purification technique where a crystalline product is obtained from a solution. In industrial practice the reactive crystallization (precipitation) process is mostly followed by solid-liquid separation processes in order to obtain a dry product. The energy required for this separation process depends mainly on the properties of the crystals. In order to minimize the energy consumption of the separation processes, it is important to control the precipitation process in a way that the crystal size of the product is maximized (Mersmann and Franke, 1993) as well as to meet the specific qualities i.e. crystal size, shape (morphology) and purity.

Precipitation is determined by a combination of processes. The mixing process results in the creation of supersaturation which is the driving force for: nucleation, crystal growth, aggregation and breakage. The hydrodynamics and chemistry of the system will influence the supersaturation, the kinetics and hence the product crystal.

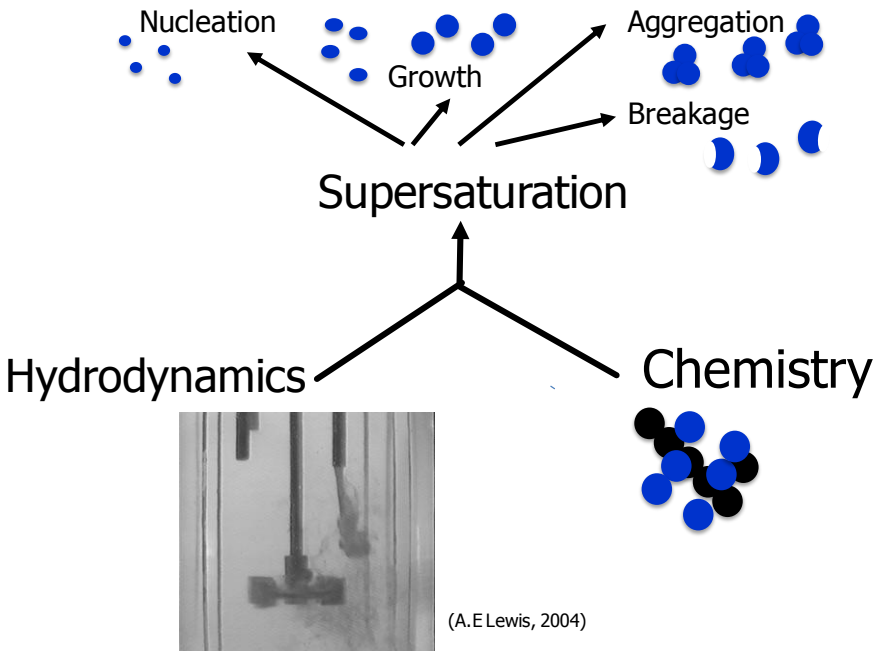

Figure 1.1 Crystallization.

The conventional reactor used in crystallization processes is the stirred tank reactor (STR). Within such a reactor, there are large variations of hydrodynamic environments, where fluid flow is inherently transient and highly turbulent (anisotropic and inhomogeneous). The turbulent energy dissipation and shear rates in these reactors are unevenly distributed consequently so are the kinetics. These large disparities in both energy and turbulence have proven to be problematic when modelling these systems.

Stirred tank reactors have very high levels of turbulence and energy dissipation rates in and around the impeller region due to the shear caused by the impeller and low turbulence and energy dissipation rates in the bulk vessel. However, oscillating grids (reactor system) produce environments with a homogeneous and nearly isotropic turbulence. Investigating and characterising crystallization kinetics in such environments can provide an essential building block to the understanding of what occurs in more complex flow systems that are experienced on an industrial scale.

1.2. Scope and limitations

Although there are numerous variables which have an effect on precipitation kinetics, in this thesis, the study of precipitation processes for sparingly soluble substances was performed for the system of calcium oxalate (CaC_2O_4). A batch oscillating multi grid mixer configuration system was used for this investigation in order to investigate the influence of turbulence on the kinetic parameters.

1.3. Thesis outline

The thesis commences with the summary of the relevant literature available on the subject matter; with a background on hydrodynamics (turbulence), various reactor geometries and the hydrodynamics associated with them. This is followed by crystallization theory of precipitation and then a review of the system used in this study. The literature of the effect of hydrodynamics on the crystallization process is also presented. A detailed description of the materials and methods used in this work follows and then the results of the study are presented and discussed. Concluding remarks on the effect of hydrodynamics on precipitation kinetics are then drawn and areas requiring further study and improvement are then presented.

Chapter 2. Literature review and theory

The aim of this chapter is to present a summary of the relevant literature available on the subject matter of this thesis. The general background theory of turbulence is presented and discussed. The theory of precipitation is also discussed and thereafter the factors that affect precipitation.

2.1. Turbulence

The conventional reactor used in numerous industrial processes including crystallisation, is the stirred tank reactor. This vessel is characterised by an impeller which is responsible for the processes of solids suspension, mixing and the generation of turbulence through agitation. Turbulence can be defined as the state of fluid motion where velocity fluctuates in time and in all directions in space (Paul *et al*., 2004).

2.1.1. Turbulent energy spectrum

Turbulent movement can be considered as a hierarchy of eddies of varying magnitudes which are determined by certain characteristic dimensions and velocities. These eddies differ in scale, with the largest eddies imposed by the geometry of the studied flow, to the smallest eddies which are imposed by viscosity.

The largest eddies take the energy directly from the mean movement, which is unstable because the critical Reynolds number has been exceeded. The first-order eddies have such a high Reynolds number, they produce eddies of the second-order. The Reynolds number associated with the second-order eddies is smaller than the first-order Reynolds number, but high enough to produce smaller and smaller eddies by non linear interaction. In this way energy is propagated to the smallest eddies. As smaller and smaller eddies are produced and energy is transferred to these eddies, the viscosity of the fluid acts and the dissipation of energy becomes larger and larger for the small eddies (Militaru, 2001).

The continual flux of energy from larger to smaller eddies results in the turbulent energy spectrum, as illustrated schematically in Figure 2.1. The energy spectrum can be thought

of as a distribution of the energy of turbulence amongst eddies of various frequencies or size. The primary eddies are the largest eddies, being of a similar scale to the impeller. The energy-containing eddies incorporate most of the kinetic energy of the system. The inertial sub-range eddies occur at high levels of turbulence and are sufficiently small to be statistically independent of the bulk and are sufficiently large to transfer significant kinetic energy through inertial forces. The viscous dissipation range eddies are the smallest eddies and contain the least kinetic energy but dissipate most of the energy of the system as heat (Militaru, 2001).

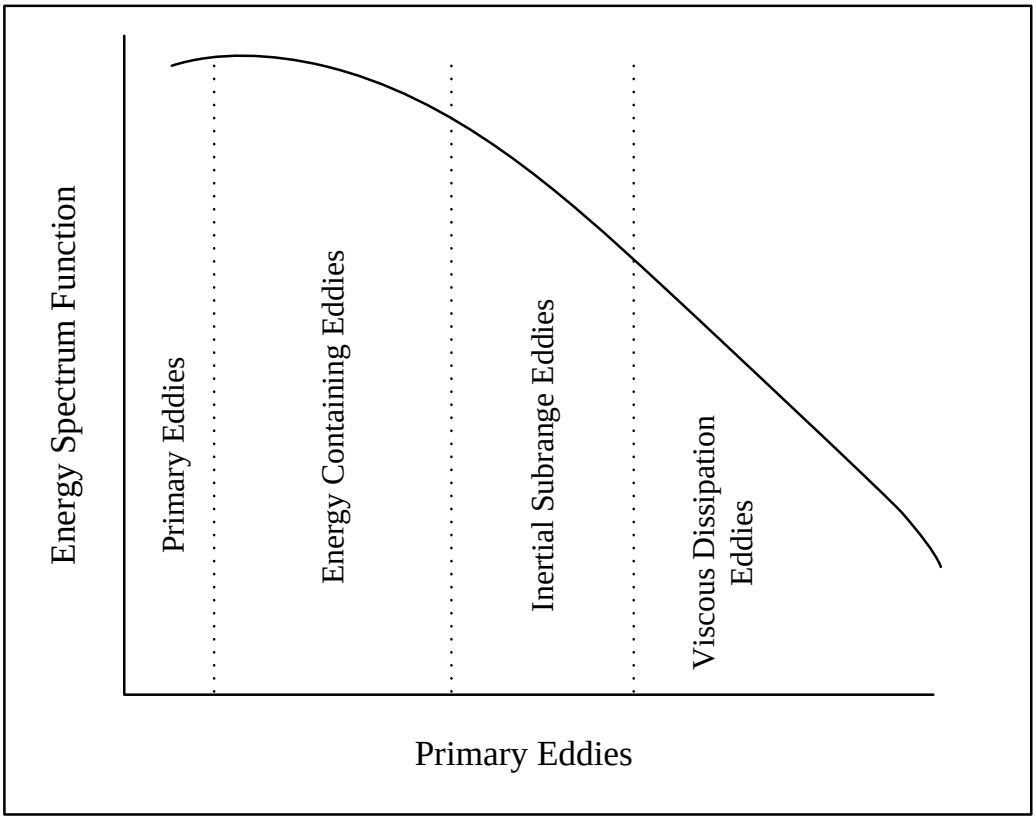

Figure 2.1 Schematic representation of a turbulent energy spectrum.

2.1.2. Turbulence parameters

Turbulence creates fluctuations in velocity. In laminar flow, the velocity at any time is the average velocity. However for turbulent flow, the velocity term includes both a mean and a turbulent component as follows:

$$v(t) = \bar{v} + u(t) \qquad 2\text{-}1$$

Where

v(t): turbulent velocity ($m.s^{-1}$)

u(t): turbulent fluctuation component ($m.s^{-1}$)

$\bar{v}$: mean velocity ($m.s^{-1}$)

The turbulent energy spectrum can be used to determine turbulence parameters commonly used for comparing and describing the level of turbulence. The integral over all frequencies of the energy spectrum function gives the mean squared turbulent velocity which is described by Equation 2-2. The square root of this quantity is termed the root mean square (RMS) turbulent velocity and it is a significant parameter that describes turbulence as it appears in both descriptions of turbulent microstuctures and theories of particle-particle collision.

$$\bar{u}^2 = \int_0^\infty E(n)dn \qquad 2\text{-}2$$

Where

$\bar{u}$: Root mean square (RMS) turbulent velocity ($m.s^{-1}$)

E: Energy spectrum function ($m^2.s^{-1}$)

n: Frequency (s^{-1})

The rate of dissipation of the turbulence energy per unit mass, ε, is a parameter that is often used to described the influence of turbulence in crystallization. The local energy dissipation in a stirred tank can vary by 10 orders of magnitude (Schubert and Bischofberger, 1998) and therefore the mean energy dissipation rate, $\bar{\varepsilon}$, is often used.

2.1.3. Homogeneous isotropic turbulence

Homogeneous isotropic turbulence is the simplest form of turbulence with a minimum number of quantities and relations required to describe it and it has often been used as a simple field to understand the effect of turbulence on mixing and can serve as a crucial building block in the understanding of more complex, real flows. Isotropic turbulence occurs when there is no spatial variation gradients in the mean squared turbulent velocity i.e. Isotropic turbulence occurs when there are no spatial gradients in the mean squared turbulent velocity i.e. $\overline{u_x^2} = \overline{u_y^2} = \overline{u_z^2} = 0$ and $\overline{u_i u_j} = 0$ (Srdic *et al*., 1996). This type of turbulence without mean shear flow, forms when a horizontal grid oscillates vertically in a homogeneous fluid.

2.1.4. Mixing

The hydrodynamic conditions that exist during precipitation play a key role in the precipitation kinetics. The hydrodynamics in a system are due to stirring of the solution and the internal construction of the precipitation vessel (reactor). Stirring increases the motion of molecules in solution and minimizes spatial variations in concentration within the solution by ensuring that the solution is well mixed.

In precipitation, reactants are brought together by mixing, hence these reactions are significantly affected by how well mixed a system is as well as how well dispersed the phases are within multiphase reactions. This is because in reactive systems, the local reactant concentration not only depends on how fast the reactants are consumed by the reaction, but also on how fast they are locally replenished from the bulk of the phases in which they initially reside.

Scales of mixing

There are generally three scales of mixing: namely micro- , meso- and macro- mixing.

Micro mixing

Micro mixing is mixing on the smallest scales of motion, the Kolmogoroff microscale, η, and at the final scales of molecular diffusivity (Paul *et al*., 2004).

$$\eta = \left(\frac{\nu^3}{\varepsilon} \right)^{\frac{1}{4}} \qquad 2\text{-}3$$

Where

η: Kolmogoroff microscale (m)

ν: fluid kinematic viscosity ($m^2.s^{-1}$)

ε: energy dissipation rate ($W.kg^{-1}$)

An increase in the turbulent intensity accelerates micro-mixing. This is because the size and length of the smallest eddies necessary to overcome diffusion resistances decreases and the micro-mixing rate only depends on the rate of engulfment, deformation and diffusion (Gradl *et al*., 2006). The characteristic time for micro-mixing is:

$$t_{micro} = 12 \left(\frac{\nu}{\varepsilon} \right)^{\frac{1}{2}} \qquad 2\text{-}4$$

Where

$t_{micro:}$ micromixing time (s)

Macro mixing

Macromixing is mixing driven by the largest scales of motion in the fluid and is characterised by the blend time in a batch. The characteristic time for macro-mixing is:

$$t_{macro} = \frac{4V}{N_q N d^3_{stir}} \qquad 2\text{-}5$$

Where

$t_{macro:}$ macromixing time (s)

V: vessel volume (m^3)

N: impeller speed (s^{-1})

d: diameter of impeller (m)

N_q: flow number (-)

Meso mixing

Another scale of mixing is meso mixing. This type of mixing occurs on a scale smaller than the bulk circulation but larger than the micromixing scales. It is most frequently observed at the feed inlet of reactors (Paul *et al*., 2004). The characteristic time for meso-mixing is:

$$t_{meso} = \frac{Q}{uD_{meso}} \qquad 2\text{-}6$$

Where

$t_{meso:}$ meso mixing time (s)

Q: volumetric flow rate ($m^2.s^{-1}$)

u: feed flow velocity ($m.s^{-1}$)

D_{meso}: turbulent diffusivity ($m.s^{-1}$)

2.2. Crystallization reactor types

For coagulation and hence aggregation measurements to be compared reliably with theoretical predictions, experimental systems must: generate well defined nearly isotropic turbulence, the initial particles need to be monodispersed and the system should be dilute to result in binary collisions dominating the aggregation process (Brunk *et al*., 1998).

2.2.1. Jar reactors

In environmental engineering literature, jar tests are often used to qualitatively understand the effect of turbulent intensity on the coagulation rate (Stumm and Morgan, 1981). However, Delichatsios and Probstein (1975) noted that the experimental conditions for jar tests are far from ideal. This is because the jar tests create a highly inhomogeneous turbulent environment, violating key assumptions of existing turbulence models. They went on and continued their studies of coagulation in turbulent pipe flow because the turbulence in such environments is well understood.

2.2.2. Plug flow reactors (Poiseuille flow)

Mumtaz and Hounslow (2000) conducted studies on the aggregation of calcium oxalate in a Poiseuille flow crystalliser (PFC). The well-characterised hydrodynamics of the PFC allows the prediction of collision rates using Smoluchowski's theory of coagulation and therefore the quantification of the efficiency of aggregation.

Poiseuille flow is the laminar flow of liquid along a cylindrical tube and it was first studied by Hagen in 1839 and Poiseuille in 1840. In this type of flow, the velocity profile in the radial direction is described by a parabola, with a maximum velocity at the centre of the tube. The shear rate is equal to zero at the centre and a maximum at the walls as depicted by Figure 2.2.

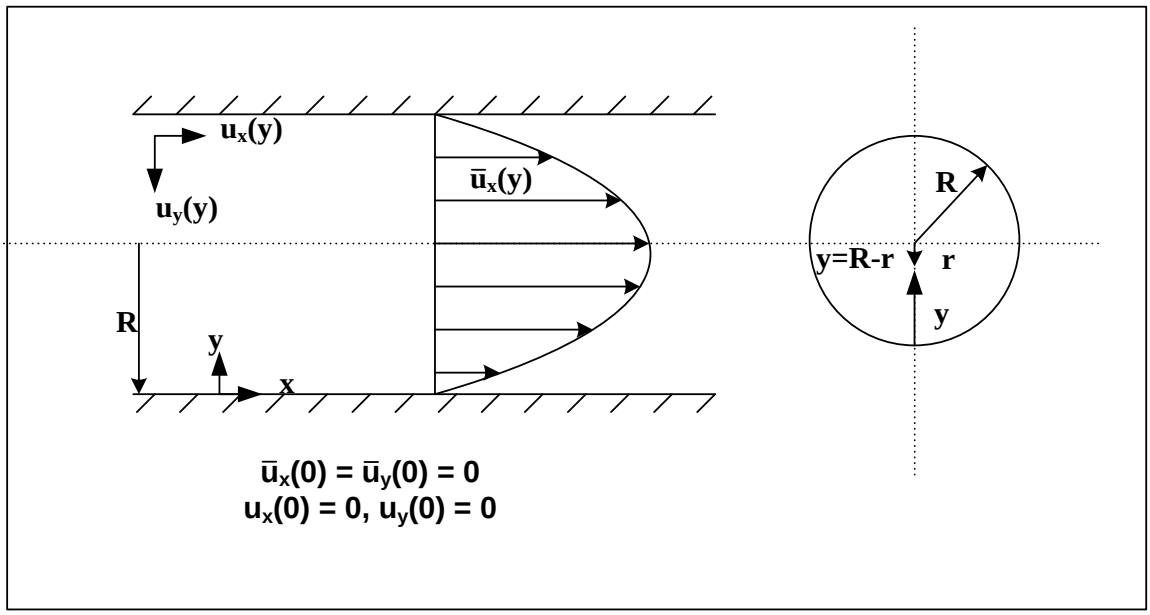

Figure 2.2 Schematic view of a turbulent pipe flow (Baldyga and Bourne, 1999).

The following equations describe the flow (hydrodynamics) in such a system:

$$u = u_{max}\left(\frac{1-r^2}{R^2}\right) \qquad \text{where} \quad u_{max} = \left(\frac{2Q}{\Pi R^2}\right) \tag{2-7}$$

$$\gamma = \gamma_{max}\left(\frac{r}{R}\right) \quad \text{Where} \ \gamma_{max} = \left(\frac{2u_{max}}{R}\right) \tag{2-8}$$

$$t_r = \left(\frac{L}{v}\right) = \frac{t_{r\,min}}{1-\frac{r^2}{R^2}} \qquad \text{Where} \ t_{r\,min} = \left(\frac{L}{u_{max}}\right) \tag{2-9}$$

Where

u , u_{max}: velocity, maximum velocity ($m.s^{-1}$)

r: radial coordinate (m)

R: internal radius of tube (m)

γ, γ_{max} :shear rate, maximum shear rate (s^{-1})

t_r, t_{rmin}: residence time, minimum residence time (s)

Mumtaz and Hounslow (2000) found that because of the well-characterised hydrodynamics in a PFC, it was possible to predict collision rates and therefore compute efficiencies, providing a much required understanding of the aggregation mechanism during precipitation.

2.2.3. Stirred tank reactors

Stirred tank reactors are used extensively in the chemical, bio chemical and mineral processing industries. They are used for gas-liquid/liquid mass transfer, for suspension of solids in chemical reactions and for blending of miscible and immiscible liquids. There are different forms of these vessels differing in shape, volume, impeller types and number of impellers.

Impellers are commonly classified as either radial impellers, producing a main radial flow perpendicular to the shaft, or axial impellers generating a flow mainly oriented parallel to the shaft. Hydrofoil impellers also exist and they typically produce strong axial flow and low shear.

In crystallization, impellers are required for solid suspension and this requires mechanical energy into the fluid-solid system by some mode of agitation. The energy input creates a turbulent flow field in which solid particles are lifted from the vessel base, dispersed and distributed throughout the liquid. This solid lifting from the base of the vessel is accomplished by lift and drag forces of the moving fluid on the solid particles and the bursts of turbulent eddies originating from the bulk flow in the vessel.

The power dissipated by an impeller rotating in a homogeneous single-phase liquid in a baffled vessel, is a function of the type of impeller and the flow regime in which the impeller operates (laminar / turbulent). This is a function of the impeller Reynolds

number, Re, and a number of geometric ratios. For an agitated vessel, the impeller Reynolds number, the power dissipation, P, and the energy dissipation per-unit liquid mass, ε, can be calculated by the following equations:

$$N_{RE} = \frac{Dv\rho}{\mu} \qquad 2\text{-}10$$

$$P = N_p \rho_L N^3 D^5 \qquad 2\text{-}11$$

$$\varepsilon = \bar{\varepsilon} = \frac{P}{\rho_L V_L} \qquad 2\text{-}12$$

Where

P: power dissipation (W)

N_p: power number (-)

ρ_L: density of liquid ($kg.m^{-3}$)

V_L: volume of liquid in vessel (m^3)

N: impeller speed (s^{-1})

N_{RE}: Reynolds number (-)

D: pipe diameter (m)

v: fluid velocity($m.s^{-1}$)

ρ: fluid density ($kg.m^{-3}$)

μ: fluid viscosity (Pa.s)

There are large variations of hydrodynamic environments within a stirred tank reactor where fluid flow is inherently transient and highly anisotropic and inhomogeneous. In addition, the turbulent energy dissipation and shear rates are unevenly distributed. This is shown by Figure 2.3.

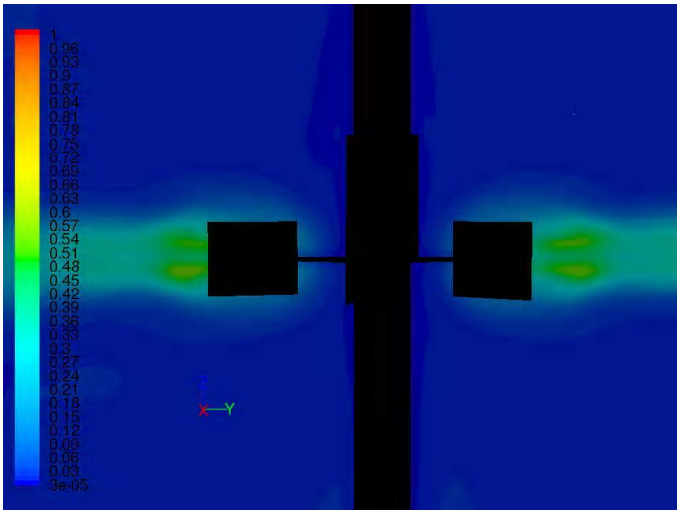

Figure 2.3 Contour plot of the turbulent kinetic energy in a stirred tank (Appa and Deglon, 2007).

2.2.4. The novel oscillating grid reactor

Section 2.2.4 is a review that was derived from the studies by Changunda, 2010.

Oscillating grids exhibit near isotropic and homogeneous turbulence, which cannot be achieved in impeller agitated tanks. In such a reactor configuration, there is no net flow direction resulting in no mean shear flow. This does not mean there is no shear present at all, but that the average shear over space and time is zero. As a result, oscillating grids can potentially provide an ideal environment to investigate the effects of energy input on precipitation kinetics.

Thompson and Turner (1975) conducted studies using a vertically oscillating one-grid configuration system. Hopfinger and Toly (1976) conducted further work and developed a law for describing the decay of turbulence in an oscillating grid system. They quantified the RMS velocity as follows:

$$u_x = u_y = \frac{C_1 M^{0.5} S^{1.5} f}{z} \qquad 2\text{-}13$$

$$u_z = \frac{C_2 M^{0.5} S^{1.5} f}{z} \qquad 2\text{-}14$$

Where

u_i: root mean square velocity ($m.s^{-1}$)

M: grid mesh size (cm)

S: grid stroke (cm)

f: grid vibrating frequency (s^{-1})

z: vertical distance (cm)

C_1, C_2: tank-geometry dependant constants; C_1, C_2 are 0.25 and 0.27 respectively

Orlins and Gulliver (2003) confirmed the above expressions by conducting tests using a two-component laser-Doppler velocimeter (LDV) system. An LDV system uses a laser, beam splitter, fibre optic probe and a signal processor to measure the velocity field inside the tank.

However, the one-grid configuration produces a bias on the RMS velocity in the direction of oscillation. To compensate for the bias produced by the one-grid configuration, the two-grid configuration became a popular choice amongst many authors, Srdic *et al.*, (1996), Shy *et al.,* (1997), and Eidelman *et al.,* (2002). The spatial decaying turbulence of both grids interacts to form a substantial nearly isotropic stationary region in between the grids which is often the domain of interest. Shy *et al.,* (1997) developed an expression for their 2-grid system which did not vary very much from the Hopfinger and Toly (1976) expression. The expression is given by:

$$u = \frac{0.89 M^{0.5} S^{1.5} f}{H^{1.5}} \qquad 2\text{-}15$$

Where

H: distance between the grids (cm)

The expression gives a good estimate of the turbulence intensity for the range $4 \le {H}/{M} \le 6$. The flow conditions to which the expression best applies is frequencies between 1 and 8Hz and a ratio of $\frac{S}{M} = \frac{2}{3}$. When the grids were widely spaced, the turbulence field was characterised by two principal zones of behaviour, an internal zone (with high turbulent flow) corresponding to the domain swept by an individual grid and a second zone (with a nearly isotropic turbulent flow region), which is away from the grid.

Srdic *et al.,* (1996) identified the effect of the grids on the turbulence. He found in the highly turbulent region near the grids $\left(1 \le {z}/{M} \le 2\right)$, the turbulence intensity was inversely proportional to the distance from the grid at the centre of the grid mesh and inversely proportional to the distance from the grid.

Matsunaga *et al.,* (1999) obtained theoretical predictions of the turbulent kinetic energy (TKE) and its dissipation rates, *ε*, for oscillating grid turbulence using the k-ε turbulence model. Janzel *et al.,* (2003) compared experimentally, their findings to those of Matsunaga *et al.,* (1999) and obtained vertical profiles of the turbulent kinetic energy with the theoretical predictions of the k-ε turbulence model and concluded that the profiles generated by the analytical solution agreed with those of the experimental turbulence kinetic energy data.

An energy balance was used to determine the energy dissipation rates per unit mass. The energy dissipation per unit mass is a principal scaling factor in the specification of nearly isotropic turbulence. The energy balance according to Bache and Rasool (1996) is defined as follows:

$P = F_{n,g}\hat{v}$ Where $F_{n,g} = F_f - F_i$ 2-16

Where

P: power dissipation (W)

$\hat{v}$: instantaneous velocity ($m.s^{-1}$)

$F_{n,g}$: net applied force to the liquid by the grid ($kg.m.s^{-2}$)

F_f : gross force in the column filled with the liquid ($kg.m.s^{-2}$)

F_i: net force in the column when empty ($kg.m.s^{-2}$)

Both F_f and F_i consider forces associated with bearings, the liquid, inertia and the weight of the shaft. However, the forces associated with bearings are minimal, inertial forces do not change and shaft weight force is non dissipative which leaves the force associated with the liquid.

Bache and Rasool (1996) went on to apply the description of the rate of energy dissipation in the boundary layer given by Batchelor (1970) to find the power lost due to skin friction, P_l. Once P_l is known, P_g, which is ultimately the effective energy on the turbulence, can be found by subtracting the power lost due to friction from the average power. The energy dissipation rate is given as follows:

$$\varepsilon = \frac{P_g}{m_l} \qquad 2\text{-}17$$

Where

P_g: power input to the grid, power lost due to skin friction (Nms^{-1})

m_l: mass of liquid in column (kg)

ε: energy dissipation rate ($W.kg^{-1}$)

Bache and Rasool (2001) advanced their work and developed an oscillating multi-grid mixer capable of generating large regions of near homogenous isotropic turbulence through the vessel. Figure 2.4 shows the variation of the RMS turbulent velocity through the vessel.

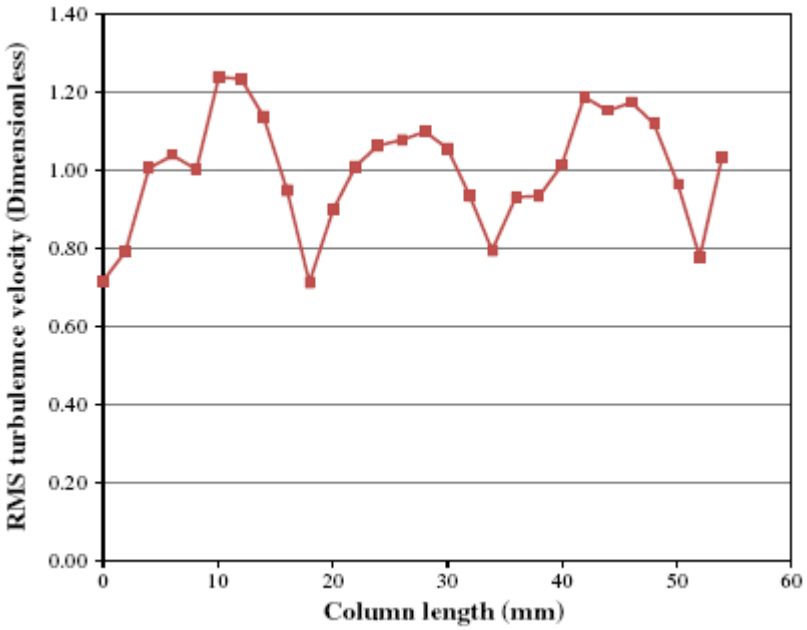

Figure 2.4: RMS turbulent velocity vs. column height for a grid frequency of 2.05 Hz (adapted from Bache and Rasool, 2001).

If the turbulence in the vessel was perfectly homogeneous, the RMS turbulent velocity would be at unity throughout. It is evident that, from Figure 2.4, the turbulence does vary throughout the vessel. The coefficient of variation of the RMS turbulent velocity is 14 % however, this is insignificant in comparison to the orders of magnitude found in stirred tanks such as Schafer *et al.*, (1997), Lee and Yianneskis (1988). Therefore, in comparison, the oscillating multi grid mixer represents a near ideal hydrodynamic environment.

2.3. Crystallization theory

Crystallization from solution is a core technology in major sectors of chemical processes and associated industries. Crystallization is an important separation process that purifies fluids by forming solids where molecules in solution or vapour are transformed into solid phase of a regular lattice structure.

2.3.1. Crystallization methods

Crystallization occurs in a thermodynamically unstable solution where the driving force for particle formation is the chemical potential or concentration of the solute in excess of its equilibrium or saturation value (supersaturation). The four types of crystallization methods from solution are: cooling, evaporative, precipitation (reaction) and anti solvent crystallization. The nature of the phase diagram of a particular system determines which method should be employed as shown by Figure 2.5

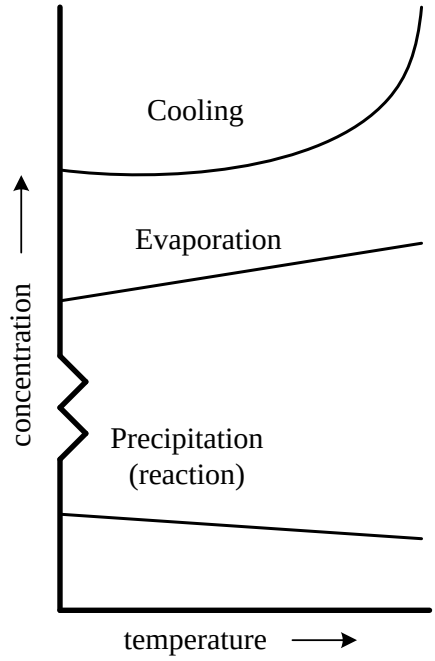

Figure 2.5 Crystallization phase diagram.

2.3.1.1. Cooling crystallization

This can either be due to direct or indirect cooling. This method is used for products with low tendencies to scale and is applied generally for medium or easily soluble substances (solubility in range of 100-300 kg/m^3). This type of crystallization is often applied to compounds where the slope of the solubility curve is positive.

2.3.1.2. Evaporative crystallization

With this method the solid product is formed by evaporation of the solvent. Evaporative crystallization is applied for easily soluble compounds (solubility in range of 10-300 kg/m^3), as a large amount of solid is formed for a given amount of evaporated solvent. It is often applied for compounds with a flat solubility curve.

2.3.1.3. Anti-solvent crystallization

The anti solvent is mixed with a concentrated solution. Crystallization occurs because the solute has a low solubility in the mixed solvent. Organic liquids are mostly used as anti-solvents, thus the water activity is lower than in the aqueous solutions.

2.3.1.4. Precipitation (reactive crystallization)

Precipitation is the crystallization of sparingly soluble substances (Söhnel and Garside, 1992) and consists of three basic steps: supersaturation, which is the driving force resulting in nucleation and growth. In nucleation and growth, two subsequent secondary processes play an important role in the determination of the final product properties (physical and chemical): aggregation and ageing. Figure 2.6 illustrates the kinetic processes mentioned above. The time scale over which precipitation takes place can vary greatly, from a few seconds to many days.

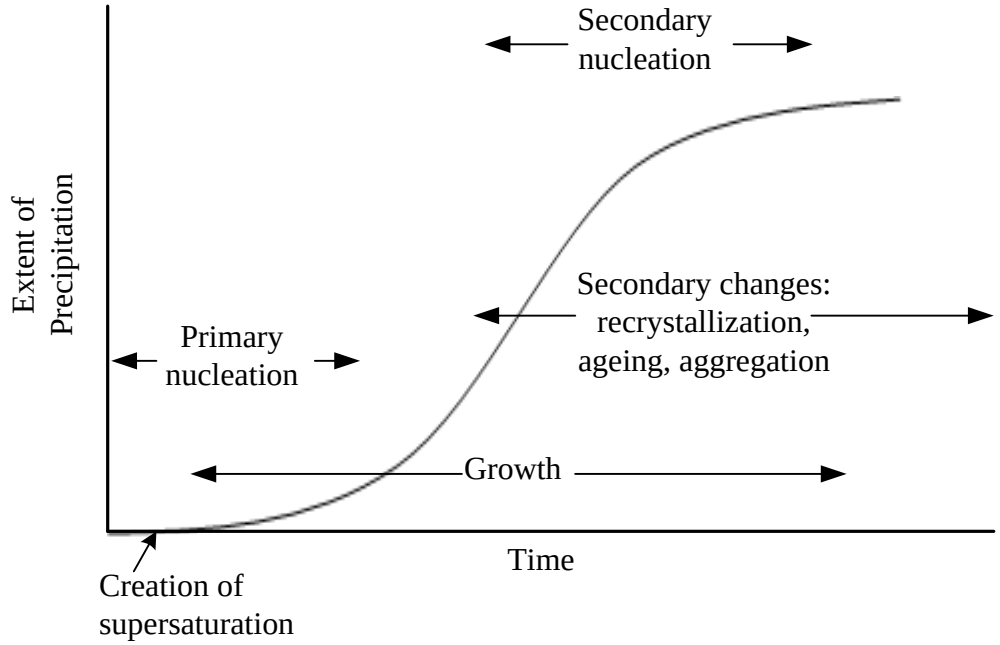

Figure 2.6 Kinetic processes involved in precipitation (Söhnel and Garside, 1992)

Precipitation differs from the other classical processes of crystallization in that the supersaturation no longer results from an action on the physical properties of the solution but rather, it is obtained by a chemical reaction between two soluble components leading to the formation of a sparingly soluble precipitate (Mersman, 2001).

In precipitation, the reaction and crystallization process occur simultaneously and they have their own kinetics which both need to be taken into consideration. This results in the study of reaction crystallization to be complex because the crystal generation depends on several processes which all have their own kinetics.

2.3.2. Supersaturation

Supersaturation is a state where the concentration of the solute in the solution exceeds the equilibrium concentration. Supersaturation controls the rates of precipitation kinetics and these kinetics ultimately influence the properties of the crystalline product formed i.e. particle size distribution and morphology.

Since supersaturation is a thermodynamically unstable condition, the concentration of ions in solution will decrease by the formation of precipitated solids until the equilibrium solubility has been restored.

There are various ways in which supersaturation can be defined. Among these, the most common expressions of supersaturation are the concentration diving force (Δc), the supersaturation ratio (S) and a quantity referred to as the absolute or relative supersaturation (σ). These quantities are defined as follows:

$$\Delta c = c - c^{*} \qquad 2\text{-}18$$

Where
c: acutal concentration($kmol.m^{-3}$)
c*: saturation concentration ($kmol.m^{-3}$)

Supersaturation is expressed in Equation 2-18 as the ratio of the activity of the ionic species to be precipitated (a_i) to the activity-based equilibrium solubility product (K_{sp}) (Myerson, 2002).

$$S = \frac{a_A a_B}{K_{sp}} \qquad 2\text{-}19$$

If
S > 1 the solution is supersaturated
S = 1 the solution is saturated
S < 1 the solution is undersaturated.

The relative supersaturation is defined as:

$$\sigma = S - 1 \qquad 2\text{-}20$$

2.3.3. Particle rate processes

2.3.3.1. Nucleation

Nucleation can be divided into two groups, namely, primary nucleation and secondary nucleation. Primary nucleation can occur through homogeneous or heterogeneous mechanisms. If a solution contains neither solid foreign particles nor crystals of its own type, homogeneous nucleation will occur at high supersaturation. If foreign particles are present, the nucleation process will be facilitated and heterogeneous nucleation will occur. These mechanisms are described pictorially by Figure 2.7.

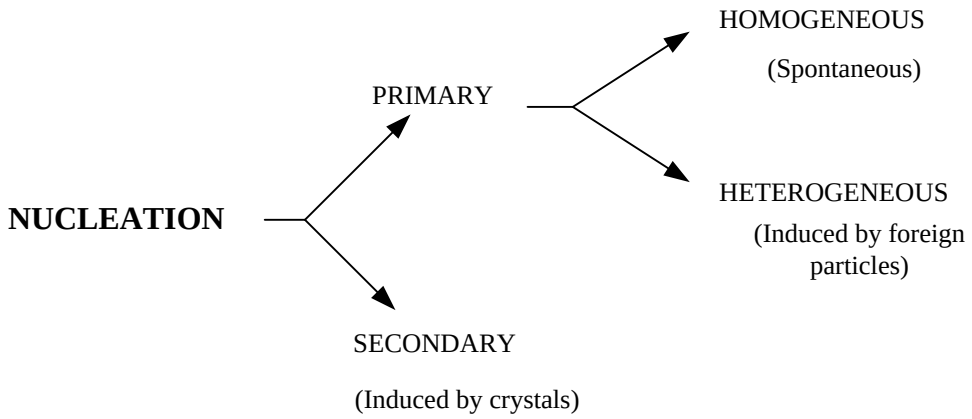

Figure 2.7 Various nucleation steps (Mullin, 1972).

A large supersaturation is the driving force necessary to initiate primary nucleation. However, supersaturation alone is not sufficient to cause a system to begin to nucleate. In order for nucleation to occur, minute solid bodies known as centres of crystallisation, seeds, embryos or nuclei have to exist (Mullin, 1972).

The initiation of primary nucleation via this driving force is not fully understood which makes it difficult to model (Mersman, 2001). Primary nucleation occurs for all cases of nucleation both, homogeneous or heterogeneous in systems that do not contain crystalline matter (occurring independently of the presence of the solid phase being precipitated). The primary nucleation rate (B^0) can be expressed by the following equation (Myerson, 2002):

$$B^0 = A \cdot \exp\left(\frac{-16\pi\sigma^3 v^2}{3k^3T^3(\ln S)^2}\right) \quad 2\text{-}21$$

Where

A: Pre-exponential factor (10^{30} nuclei.cm^{-3}.s^{-1})

σ: Surface Tension (dynes.cm^{-1})

υ: Molecular volume (cm^3.g^{-1})

k: Boltzmann constant (1.38e^{-23} m^2.kg.s^{-2}.K^{-1})

T: Temperature (K)

S: Supersaturation ratio (-)

In addition it is noted that Equation 2-20 indicates that the rate of nucleation will increase with increasing supersaturation and temperature and decreasing surface tension.

The second principle mechanism in crystallization is secondary nucleation. In this phase of crystallization, crystal growth is initiated with contact. The contact can be between the solution and other crystals, a mixer blade or a vessel wall. This phase of crystallization occurs at lower supersaturation (than primary nucleation) where crystal growth is optimal. The secondary nucleation rate (B) can be expressed by the following equation (Jones, 2002):

$$B = E_t F_1 F_2 \quad 2\text{-}22$$

Where

E_t: rate of energy transfer to the particles

F_1: production function

F_2: survival function

F_1 is the product function and it gives the number of particles generated per unit of transferred energy. F_2 is the survival function and it gives the fraction of particles that survive to become nuclei and subsequently grow to populate the size distribution.

If these nuclei are produced by crystal collisions, E_t is defined as follows:

$$E_t = \int_0^{\infty} E(L)f(L)n(L)dL \qquad 2\text{-}23$$

Where
E(L): collision energy
f(L): collision frequency

Different approaches have been used to estimate for E(L) and f(L), both for particle impacts and turbulent fluid induced attrition.

Secondary nucleation can occur due to the following mechanisms:

- Initial breeding – occurs if dry seed crystals are introduced into a solution,
- Dendritic breeding – occurs due to particle disruption,
- Attrition breeding by contact nucleation - occurs due to particle impact or fluid flow,
- Fluid shear breeding – occurs due to turbulent fluid shear forces exerted on the crystal surface.

2.3.3.2. Growth

Crystal growth occurs as soon as stable nuclei (particles larger than a critical size) have been formed in a supersaturated or super cooled system (Mullin, 1972). The mechanism and the rate of crystal growth can be categorised into two groups: adsorption and diffusion.

Growth limited by mass transfer (diffusion)

This is the transfer of precipitating ions through a stagnant diffusion layer surrounding the crystal surface (assuming the bulk solution is perfectly mixed). The crystal growth rate (rate of crystal mass increase) using the diffusion layer model is represented by the following equation (Myerson, 2002):

$$\frac{dm_c}{dt} = k_d A(C_b - C_i) \qquad 2\text{-}24$$

Where

C_b: bulk solute concentration ($mol.m^{-3}$)

C_i: solute concentration at the solid-liquid interface ($mol.m^{-3}$)

k_d: mass transfer coefficient ($m.s^{-1}$) (accounts for fluid dynamics and solution properties)

A: crystal surface area (m^2)

In addition it is noted that Equation 2-23 indicates that crystals which have a smaller surface area (smaller crystals) seem to grow slower than larger crystals.

Growth limited by surface deposition

This is the process by which growth units of the crystallizing material are incorporated into the crystal lattice after they have been transported to the crystal surface. This process comprises of various stages. The growth unit first adsorbs on the crystal surface and part of its salvation shell is then released, after which the growth unit diffuses in the adsorption layer. This unit then can either reach a point where it is incorporated into the lattice or leave the adsorption layer and return to solution (Söhnel and Garside, 1992). The growth rate (G) for this step can be represented by a simple power law expression obtained from Myerson (2002):

$$G = k_i \cdot (C_i - C_{eq})^m \qquad 2\text{-}25$$

Where

k_i: surface reaction rate constant ($kmol^{1-m}m^{3m-2}s^{-1}$)

C_i: solute concentration at the solid-liquid interface ($mol.m^{-3}$)

C_{eq}: solubility of the precipitating species ($mol.m^{-3}$)

m: order of the surface reaction

If mass transfer limitations are negligible, then it can be seen that the supersaturation level influences the growth rate as C_i approaches the bulk solute concentration (C). A pictorial representation of these two stages is shown in Figure 2.8 where various concentration driving forces can be seen.

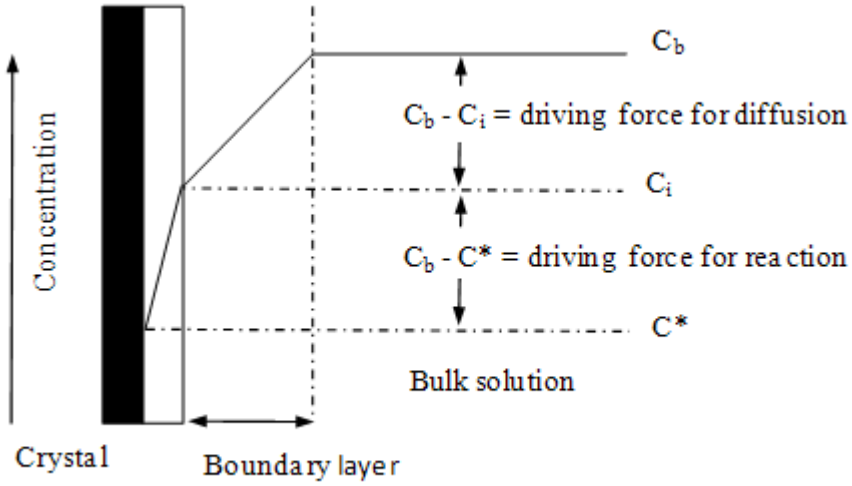

Figure 2.8 Concentration profiles during crystal growth (Mersmann, 2001).

Where

C^*: concentration at the crystal surface ($mol.m^{-3}$)

2.3.3.3. Aggregation

Aggregation is a particle enlargement process where two or more particles collide and cement together by crystal growth (by a crystalline bridge between the two particles or more crystals) to form a new, larger particle (Mumtaz and Hounslow, 2000). The rate of aggregation and break up of these aggregates depends on mechanical and fluid dynamic processes, such as the movement of primary particles, kinetic processes, crystal growth in supersaturated solutions and particle properties (Mersman, 2001). In addition to these, turbulence induced forces and other inter-particle forces such as the Van der Waals forces act on the particles and determine the extent of attachment of these particles to form stable aggregates. Aggregation can occur through two types of mechanisms, namely, primary or secondary aggregation. These mechanisms are shown graphically in Figure 2.9.

Primary aggregation

Primary aggregation occurs as a result of malgrowth of crystals (polycrystals, dendrites, and twins) and is believed to arise either as a consequence of impurity action or by diffusion field limitations (Jones, 2002 and Mersman, 2001).

Secondary aggregation

Secondary aggregation occurs as a result of crystal-crystal collisions**.** There are three types of secondary aggregation: perikinetic aggregation due to Brownian motion of small particles (<1μm), orthokinetic aggregation due to larger particles (>1μm) and inertial aggregation due to gravitational or inertial forces.

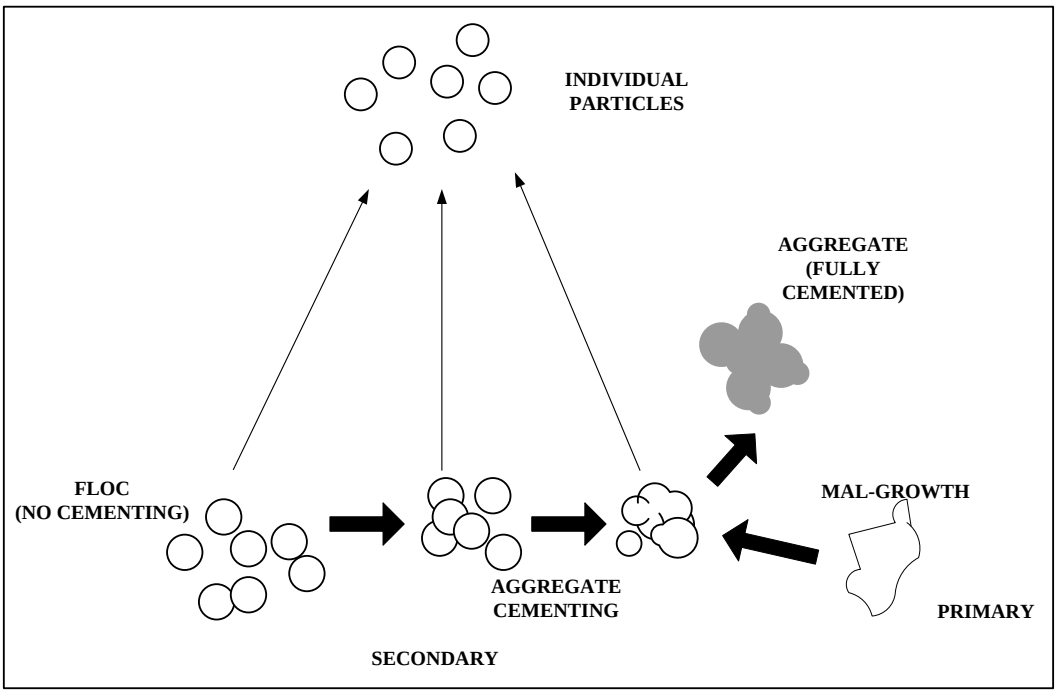

Figure 2.9 Schematic diagram of aggregation processes (Jones, 2002).

Transport and collision of particles

The collision between particles in turbulent fluids is important for many industrial processes. Particle-particle collisions are controlled largely by hydrodynamic forces and can be envisaged by the principles of fluid dynamics. Turbulent collisions drive the aggregation of solid particles which is important to industrial processes such as wastewater treatment and crystallization

processes (Shuetz & Piesche, 2002). A number of mechanisms exist for particles to collide. Three mechanisms that can occur in turbulent systems are depicted in Figure 2.10.

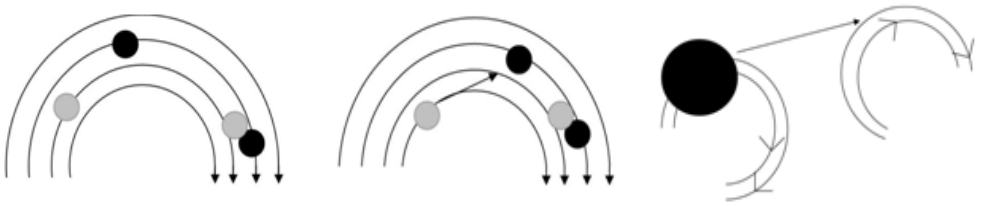

(i) Shear mechanism (ii) Accelerative mechanism (iii) Purely accelerative mechanism

Figure 2.10 Collision models in turbulent conditions.

i) The *shear mechanism* is because of the spatial variation of turbulence which assumes that particles follow fluid motion without deviation;

ii) The *accelerative mechanism* accounts for the inertial effects in turbulent collision. Particle and fluid velocities are poorly correlated so that the heavier particles will deviate from their streamline due to gravity and collide with inertia-less particles;

iii) The *purely accelerative* mechanism accounts for large particles or a vigorous turbulent flow. The particles may no longer be dragged by the smaller eddies (inertial sub-range), i.e. at high Stokes number, particle motion is completely uncorrelated with the fluid. In this case, particles will be able to acquire enough momentum to be projected from an eddy to another neighbouring eddy.

The collision rate can be defined as the product of the square of the particle number concentration and a rate constant or kernel:

$$r_{coll} = \frac{1}{2}\beta_{coll} m_0^{\,2} \qquad \text{Where} \qquad \beta_{coll} = f(\bar{\varepsilon}, L_i, L_j) \qquad 2\text{-}26$$

Where

$L_{i,}\, L_j$: size of particles (m)

ε: local energy dissipation rate ($m^2.s^{-3}$)

m_0: particle concentration ($\#.m^{-3}$)

Three dimensional turbulent flow is considered in this work hence, defining a one dimension velocity gradient will be incorrect. It is assumed that the fluid deformation rate can be taken as a measure for the velocity gradients found in the fluid. Staffman and Turner (1956) formulated the total collision kernel for two particles 1 and 2 as:

$$\beta_{coll} = \left(\frac{8.\pi}{3}\right)^{0.5} (r_1 + r_2)^2 \left[\underbrace{3\left(1 - \frac{\rho_1}{\rho_s}\right)(\tau_1 - \tau_2)^2 \overline{\left(\frac{\partial}{\partial t} v_1\right)^2}}_{\text{acceleration}} + \underbrace{3(r_1 + r_2)^2 \frac{\varepsilon}{v}}_{\text{shear}} \right]^{0.5} \qquad 2\text{-}27$$

Where τ_i (for particles obeying Stokes law) is defined as:

$$\tau_i = \frac{(2\rho_s + \rho_l) r_i^{\,2}}{9\eta} \qquad 2\text{-}28$$

And $\overline{\left(\frac{\partial}{\partial t} v_1\right)^2}$ is defined as

$$\overline{\left(\frac{\partial}{\partial t} v_1\right)^2} = 1.16 \varepsilon^{\frac{3}{2}} v^{\frac{-1}{2}} \qquad 2\text{-}29$$

The overall aggregation rate is a function of collision frequency and the aggregation efficiency, which takes into account the disruptive hydrodynamic shear forces hence the overall aggregation rate is defined as:

$$\beta_{agg} = f(\bar{\varepsilon}, S)\beta_{coll}(\bar{\varepsilon}, L_i, L_j) \quad 2\text{-}30$$

In a multi particle system, the aggregation rate, $r_{agg}(L,\lambda)$, at which the particles of size [L, L+ d L] aggregate with particles of size [λ, λ + d λ] is proportional to the product of the number of particles in these respective size ranges. The aggregation kernel $\beta(L, \lambda)$, is often used to characterise the rate of aggregation and it is the measure of the frequency with which a particle of size L aggregates with one of size λ. Therefore,

$$r_{agg}(L,\lambda) = \beta(L,\lambda)\partial N_L \partial N_\lambda \quad 2\text{-}31$$

The above equation implies that all collisions are binary in nature. It is proposed that the aggregation kernel is the product of two factors, and the kernel is written in the format below.

$$\beta(L,\lambda) = \beta_0 f(L,\lambda) \quad 2\text{-}32$$

β_0 depends on the operating conditions such as fluid velocity and the chemical environment and is independent of particle size while the second factor, $f(L, \lambda)$ is a function of particle size.
Table 2.1 shows a list of various kernels (size dependent and size independent) used to model aggregation during precipitation (Bramley *et al.*, 1996).

Table 2.1 Aggregation kernels.

Size-independent	β_0
Brownian motion	$\beta_0(L + \lambda)(L^{-1} + \lambda^{-1})$
Gravitational	$\beta_0(L + \lambda)^2\lvert L - \lambda\rvert$
Shear	$\beta_0(L + \lambda)^3$
Particle inertia	$\beta_0(L + \lambda)^2\lvert L^2 - \lambda^2\rvert$
Thompson Kernel (empirical)	$\dfrac{\beta_0(L^3 - \lambda^3)^2}{(L^3 + \lambda^3)}$

Particle interactions

After the particles have collided, the combination of the external and inter-particle forces will determine whether the formation of an aggregate will occur. The main attractive forces acting on the particle are the London-Van der Waals forces (Ayazi-Shamlou and Tichener, 1993). The repulsive forces are mainly due to the electric double layer present on the particles.

Rupture of aggregates

The disruption / breakage of aggregates in turbulent flow occurs either by collision mechanical break up or by turbulent fluid mechanical break up (Ayazi-Shamlou and Tichener, 1993). Binary breakage is normally assumed which is reasonable since it can be imagined that only one breakage event occurs in an instant. Multiple particle breakage may be regarded as a result of several events of two-body breakage.

Ayazi-Shamlou and Tichener (1993) found the rate of disruption to be equal to the number concentration of the aggregates, the frequency of disruption by instantaneous stress and the number of particles eroding from the aggregate per collision. In a stirred vessel, the disruption rate is expected to be proportional to the mean dissipation rate per unit mass, ε, in the viscous subrange and to ε^2 in the inertial sub range.

Kramer and Clark (1999) studied the breakage of larger aggregates from hydrodynamically induced collisions of smaller particles. They found that the mechanism of aggregate disintegration is force or stress-inducing rupture or fracture within the body of the material. However, it must be noted that a complete mechanistic understanding of particle breakage is not available.

Aggregation cementation

The cementation rate is directly related to the growth rate and consequently strongly dependent on supersaturation. This has been experimentally corroborated in many systems by authors such as Bramley *et al.,* (1996).

2.3.4. The effect of supersaturation on nucleation and growth mechanisms

Homogeneous nucleation (spontaneous nucleation) occurs at high degrees of supersaturation (Söhnel and Garside, 1992). Under these conditions, large nuclei are formed and nucleation is the dominant process, resulting in the formation of flocculated colloids. Crystal growth is favoured in the lower region of supersaturation because crystal growth rates are dominant than primary nucleation because fewer nuclei are formed. The above mentioned mechanism is illustrated pictorially in Figure 2.11.

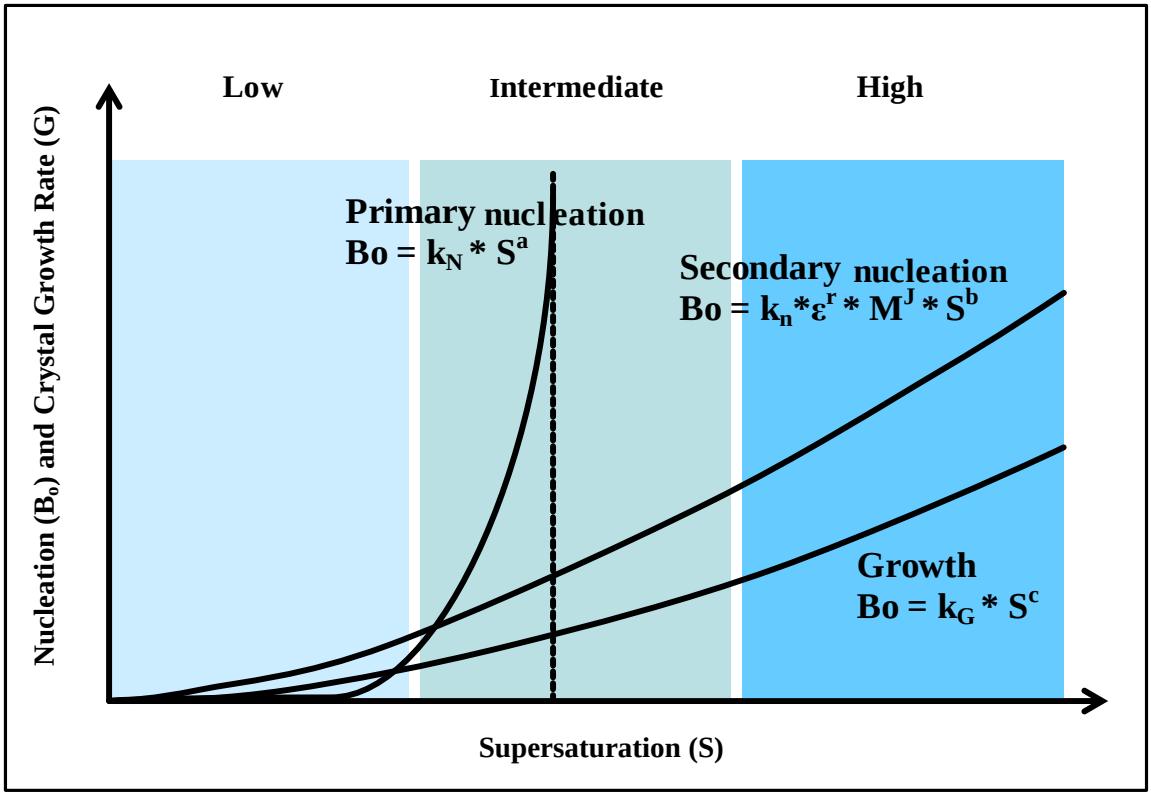

Figure 2.11 The effect of supersaturation on nucleation and growth rates (Scholz, 2006).

2.4. The influence of hydrodynamics on precipitation

Chemical reactions and nucleation kinetics within precipitation processes are often very fast (Garside and Tavare, 1985). Thus in many precipitation processes, turbulent mixing is very important and contributes significantly to the distribution of supersaturation throughout the vessel. Since supersaturation is the main driving force for nucleation, growth and aggregation

mixing has a strong impact on the product properties such as particle size distribution, surface area and particle morphology.

2.4.1. Supersaturation

Good mixing of the reactant feed stream with the bulk solution of the precipitation vessel is essential to achieve good overall mixing in the system and to smooth out any supersaturation peaks in local regions (Mullin, 2001).

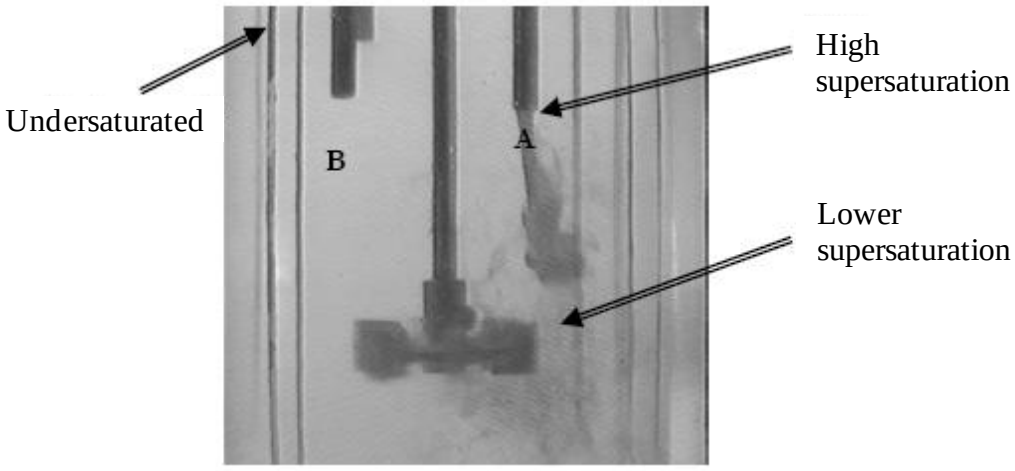

Figure 2.12 The effect of hydrodynamics on supersaturation in a stirred baffled reactor (Vicum *et al*., 2004).

Figure 2.12 shows a precipitating reagent, A, being introduced into a bulk solution, B, in a fed batch system. The plume of reagent is visible, indicating inefficient mixing. The supersaturation along the boundary of the feed plume close to the entry point is high and this is because the concentration of the feed reagent is the highest. In the impeller region, the supersaturation is decreased because the concentration of the feed reagent is distributed due to agitation. In the bulk zone (away from feed regions and impeller region) the region is undersaturated because the effect of mixing is not yet significant.

2.4.2. Nucleation

Primary nucleation may be induced by mixing but the effects of mixing on true primary nucleation are extremely complex. It has been observed that there is a reduction in the

metastable width in a static system compared to that of an agitated system. Secondary nucleation is mixing dependent as follows:

- Crystal – crystal impact: this is a function of both local micromixing environment and the overall macromixing circulation,
- Crystal – impeller and crystal- wall impact : these are functions of impeller speed, shape of blade and material of construction,
- Adsorbed layer – the thickness is decreased by an increase in mixing (Paul *et al.*, 2004).

2.4.3. Growth

Growth is affected by mixing in the following ways:

- The mass transfer rate in the diffusion film around the crystals,
- The bulk turnover rate and its effect on minimizing differences in the supersaturation ratio throughout the vessel,
- The effect of shear on crystal breakage,
- The growth rate dispersion (Paul *et al.*, 2004).

2.4.4. Aggregation

The fundamental understanding of processes leading to aggregation in turbulence is limited. During the years, a variety of turbulent models have been proposed (Staffman and Turner, 1956; Delichatsios and Probstein, 1974; Hartel *et al*., 1986; Brunk *et al*., 1997; Houcine *et al*., 1997; Bramley *et al*, 1997; Mumtaz and Hounslow, 2000), however, without well-controlled experiments that satisfy the assumptions of the various models.

Mixing enhances the frequency of particle collision (Kruis and Kuster, 1997; Staffman and turner, 1956; Delichatsois and Probstein, 1974) which drives the aggregation process. It has been found that, at low shear rates, hardly any collisions take place even though the efficiency of collisions is high. This leads to the aggregation rate constant to be small. In addition, due to the efficiency being close to unity at these low shear rates, the aggregation rate constant varies linearly with shear rate. This observation was first found by von Smoluchowski (1917) who investigated aggregation to determine the collision frequency as well as Mumtaz and Hounslow (2000). At very high shear rates (vigorous mixing) numerous collisions take place, but the

hydrodynamic tensile forces are so great they results in shorter time scales for bridge formation. This results in larger stresses in the bridge between particles. As a result, none of these collisions result in the formation of a stable aggregate and a decrease in aggregation. The consequence of these two opposing mechanisms is a maximum in the aggregation rate.

2.5. Population balance

2.5.1. Introduction

The population balance describes the way the crystal size distribution develops in time as a result of the various kinetic processes. The population balance for a well mixed crystallizer, as given by Randolph and Larson (1962) is:

$$\frac{\partial(n(L,t)V(t))}{\partial t} = -V\frac{\partial(G_L(L,t)n(L,t))}{\partial t} + B(L,t)V - D(L,t)V + \sum_{j=1}^{m}\phi_{v,in,j}(t)n_{in,j}(L,t) - \sum_{k=1}^{n}\phi_{v,out,k}(t)h_{out,k}(L,t)n(L,t)$$

2-33

The amount and the size of particles is expressed in terms of the number density n(L,t) [#/m^3] and particle length L [m]. V [m^3] is the crystallizer volume and m [-] streams entering and n [-] streams leaving the crystallizer with volumetric flow rates φ_v [m^3/s]. G_L(L,t) [m/s] is the linear size independent growth rate, and D(L,t) and B(L,t) [1/(m^3ms)] are the death rates respectively.

Since the above population balance equation is a partial differential equation with respect to time, t[s] and crystal length, [m], the boundary equations necessary to solve the equation are:

$$n(0,t) = \frac{B_0(t)}{G_L(0,t)}$$

2-34

n(L,0) = initial distribution

2-35

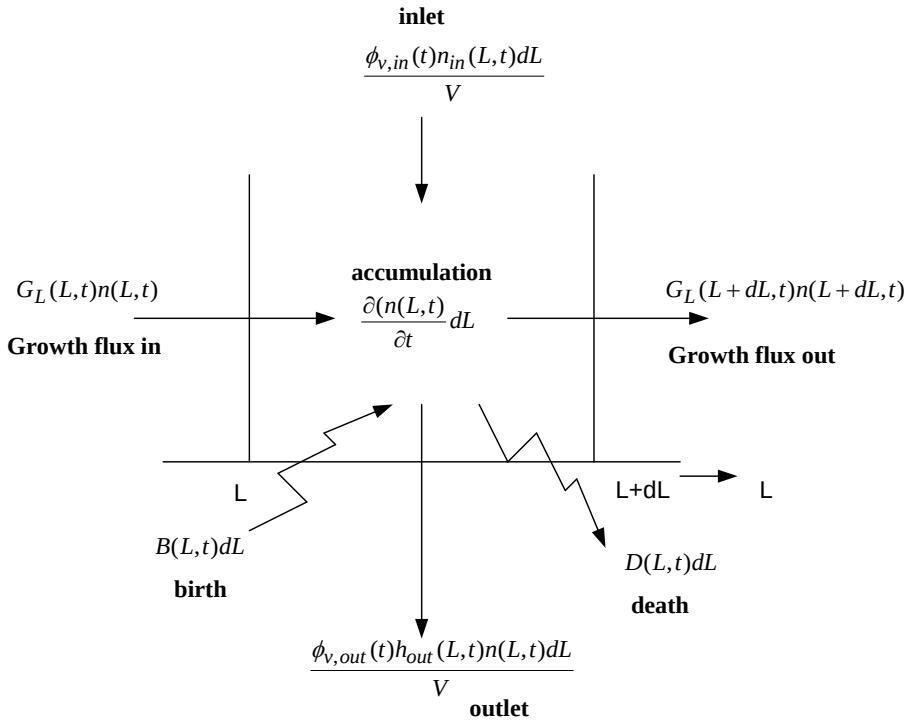

Figure 2.13 Schematic diagram of processes affecting crystal size distribution (Lewis *et al.*, 2008).

- $\frac{\partial(G_L(L,t)n(L,t))}{\partial t}$,

represents the size dependent growth of particles. If the growth rate is independent of particle length the above term reduces to $G_L(t)dn(L,t)/dL$.

- $B(L,t)V - D(L,t)V$,

describes the birth and death of particles of a particular size as a result of aggregation, breakage and nucleation.

- $\sum_{j=1}^{m}\phi_{v,in,j}(t)n_{in,j}(L,t)$,

represents the number of inlet streams which may or may not contain a population of particles.

- $\sum_{k=1}^{n} \phi_{v,out,k}(t) h_{out,k}(L,t) n(L,t)$

describes the number of outlet streams with crystal size distributions which, depending on the hydrodynamic conditions within the vessel, may be similar or different to the crystal size distribution within the vessel. The relationship between the difference within the vessel and that of an outlet stream is normally described by the classification function, h(L).

Secondary and primary nucleation involves the birth of small crystals. Instead of the birth term in the population balance equation describing the birth of new crystals B(L,t) over a certain size range ($0 \leq L \leq y$), the birth term in the first boundary condition (Equation 2.32) may be used, $B^0(t)$.

The relation between the two terms of nucleation, B(L,t) and $B^0(t)$ is:

$$B^0(t) = \int_0^y B(L,t)dL \qquad 2\text{-}36$$

For a well-mixed batch system at constant volume, the population balance becomes:

$$\frac{\partial n}{\partial t} + G\frac{\partial n}{\partial L} = B(L) - D(L) \qquad 2\text{-}37$$

Where $\partial n/dt$ gives a change in the number density with respect to time in the batch crystallizer, $G\partial n/dL$, describes the difference between crystals growing in and out of a size interval L to L+dL. The parameters B and D represent the birth and death rates respectively due to nucleation, aggregation and breakage. The number density function, n (L) is defined by equation 2-37 and it can be calculated from a volume based histogram of vol% vs. L_i using equation 2-38.

$$n(L) = \frac{dN}{dL} \qquad 2\text{-}38$$

$$n(L)dL = \sum_i \frac{vol\% \times conc(vol\%)}{100} \frac{1}{k_v L^3} \qquad 2\text{-}39$$

Where

conc (vol%): particle concentration

k_v: volume shape factor, equal to $\pi/6$

2.5.2. Moment transformations

When growth and aggregation occur at the same time, a complete analytical solution to the population balance is not possible. Another technique can be used to overcome this problem which uses the moments of the particle size distribution. These moments are obtained by integrating the number density n(L) with respect to the size of the particle, L. The j_{th} moment to its internal coordinate is defined by Randolph and Larson (1988) as:

$$\frac{dm_j}{dt} - jGm_{j-1} = \overline{B_j} - \overline{D_j} \qquad 2\text{-}40$$

The first four moments provide useful properties of the particle size distribution. The zeroth moment, m_0 (m^{-3}), is equal to the total number of particles, the first moment, m_1 ($m.m^{-3}$), the second moment, m_2 ($m^2.m^{-3}$) and the third moment, m_3 ($m^3.m^{-3}$) are proportional to length of particles, the total surface area of the particles and the total volume of particles respectively. These moments and their dimensions are shown in Table 2.2 and Table 2.3.

Table 2.2 The meaning of the various moments of a crystal size distribution in terms of length.

property	definition	dimension
m_0	total number of particles per unit crystallizer volume	$1/m^3$
m_1	total length of particles per unit crystallizer volume	m/m^3
m_2	related to the total surface area of particles per unit crystallizer volume	m^2/m^3
m_3	related to the total volume of particles per unit crystallizer volume	m^3/m^3

Table 2.3 Properties of the distribution based on the moments.

Property	definition	dimension
total number	$N_T = m_0$	$1/m^3$
total length	$L_T = m_1$	m/m^3
total surface area	$A_T = k_a m_2$	m^2/m^3
total volume	$V_T = K_v m_3$	m^3/m^3
mean (number based)	$L_{1,0} = m_1 / m_0$	m
mean (mass / volume based)	$d_{4,3} = m_4 / m_5$	m
coefficience of variace (mass based)	$CV = (m^3 m^5 / m_4^2)^{½} - 1$	-

2.5.3. Precipitate formation mechanism

Assuming size independent growth and aggregation and the absence of breakage, the molecular growth rates, G_0, aggregation kernel, β_0, and the aggregation rate, R_a are given by the following equations respectively (Randolph and Larson, 1988):

$$G_0 = \frac{\Delta m_3}{3\Delta t \overline{m_2}} \qquad 2\text{-}41$$

$$\beta_0 = \frac{\Delta m_2}{3\Delta t\left(\overline{m_1}\right)^2} - \frac{2G_0}{\overline{m_1}} \qquad 2\text{-}42$$

$$R_a = -\frac{\beta_0 m_0^{\,2}}{2} \qquad 2\text{-}43$$

(Rewritten for the case of constant volume)

Where

Δm_2: change in the second moment

m_0: zeroth moment

$\overline{m}_1, \overline{m}_2$: first and second moments respectively

2.6. Precipitation kinetics of calcium oxalate

2.6.1. Introduction

The system that is studied in this thesis is that of calcium oxalate. Calcium oxalate is a naturally occurring inorganic salt relevant to kidney stone research, however it was chosen in this study for reasons of extensive research conducted on this compound. This will allow the results obtained in this work to be compared with previous studies.

Calcium oxalate exists in several morphologies and forms depending on conditions of formation. These conditions are molar concentrations, buffering, pH, stirring and temperature. There are three hydrate forms of calcium oxalate that are crystallized with different morphologies namely:

- Calcium oxalate monohydrate, $CaC_2O_4.1H_2O$, (COM) which precipitates in the monoclinic, prismatic or hexagonal or dendrite form,
- Calcium oxalate dihydate, $CaC_2O_4.2H_2O$, (COD) which precipitates in the tetragonal, bypiramidal shape,
- Calcium oxalate trihydrate, $CaC_2O_4.3H_2O$, (COT) which precipitates as triclinic or needle shape (Thongboonkerd *et al*., 2005).

The most stable hydrate, $CaC_2O_4.1H_2O$, is a poorly soluble compound. In water at 25 °C its solubility product, K_{sp}, is = $2.0x10^{-9}$ $mol^2.l^{-2}$ and at 37 °C the K_{sp} = $2.8x10^{-9}$ $mol^2.l^{-2}$. Under these conditions the solubility is equal to 0.00065 mass% which is $4.0x10^{-5}$ $mol.l^{-1}$ and 0.00077 mass% which is $5.3x10^{-5}$ $mol.l^{-1}$.

2.6.2. Kinetics

The precipitation of calcium oxalate is normally done in batch mode (seeded). Calcium oxalate can be synthesised from calcium chloride ($CaCl_2$) which provides the calcium ions and form sodium bicarbonate (Na_2CO_4) which provides the oxalate ions. Extensive studies conducted on this system have resulted in the growth kinetics being well

understood. Studies conducted in a Poiseuille flow crystallizer have shown that growth of calcium oxalate is independent of crystal size and dependent on supersaturation and in turn on the composition of the solution (Mumtaz and Hounslow, 2000). This also agrees with work conducted by Bramley and co-workers (1997) where precipitation was conducted in an agitated batch system.

2.6.2.1. Nucleation

Literature on the nucleation of calcium oxalate monohydrate is not extensive because most studies are conducted to observe growth and aggregation.

The nucleation rates calculated for this system cover the range from 5.6×10^{8} to 2.8×10^{11} $m^{-3}s^{-1}$. Garside *et al.,* (1982) found nucleation rates from 2.78×10^{7} to 8.33×10^{7} $m^{-3}s^{-1}$ at 37°C and 0.001 M feed concentration, and those calculated from the data of Brown and co-workers (1991) are between 2.78×10^{4} and 2.7×10^{10} $m^{-3}s^{-1}$ also at 37°C.

The shorter the residence time, the higher the nucleation rate becomes, which is in agreement with high supersaturation levels at short residence times. Different stirrer speeds lead to different distributions of the supersaturation and therefore to inhomogeneities and steep local gradients in the nucleation rates. Therefore studying nucleation rates by varying the stirrer speed in a stirred reactor is not a suitable approach for determining fundamental nucleation kinetic data. Söhnel and Garside (1992) describe other methods to calculate the nucleation rate such as turbidity and induction time measurements.

Brown and co-workers (1991) published data that can be used to model primary nucleation kinetics. These authors measured the change in turbidity and related the nucleation kinetics to the supersaturation ratio leading to the kinetic expression:

$$B^{0} = 9.38 \times 10^{11} e^{\frac{52.09}{\ln^{2} S}} \qquad 2\text{-}44$$

2.6.2.2. Molecular growth

For sparingly soluble crystals (<20μm) or for well mixed suspensions, the diffusion of material to the surface is rapid and the surface reaction is likely to be the rate limiting step in the growth process (Collier and Hounslow, 1999). In this work, all of the above conditions are true hence it is assumed that the crystal growth is limited by the surface reaction. There are numerous postulated surface growth mechanisms of which the commonly proposed controlling mechanisms are: surface adsorption, spiral growth and surface nucleation. The following expressions describe these mechanisms respectively:

$$G = K_1(S-1) \qquad 2\text{-}45$$

$$G = K_2(S-1)^2 \qquad 2\text{-}46$$

$$G = K_3 S^{\frac{7}{6}}(S-1)^{\frac{2}{3}}(\ln S)^{\frac{1}{6}}\exp\left(\frac{-K}{\ln S}\right) \qquad 2\text{-}47$$

Where

$$S = \left(\frac{AP}{K_{sp}}\right)^{\frac{1}{2}} = \left(\frac{a_{Ca^{2+}}a_{C_2O_4^{2-}}}{K_{sp}}\right)^{\frac{1}{2}} = \left(\frac{\gamma_{\pm}\left[Ca^{2+}\right]\gamma_{\pm}\left[C_2O_4^{2-}\right]}{K_{sp}}\right)^{\frac{1}{2}}$$

Bramley and co-workers (1997) explained the growth mechanism for calcium oxalate by a parabolic rate law suggesting a surface spiral mechanism. The rate equation expression is shown in equation 2-47:

$$G = k(S-1)^2 \qquad \text{Where } k = 1.32 \times 10^{-9} \qquad 2\text{-}48$$

2.6.2.3. Aggregation

Hounslow, *et al*., (1988) and Bramley *et al*.,(1996) concluded that the kernel that describes their experimental results obtained from batch and continuous crystallizers, is the simplest of all, the size independent aggregation kernel (refer to section 2.3.3.3 for different types of kernels).

Hartel *et al*., (1986), Houcine *et al*., (1997) and Bramley *et al*, (1997) conducted experiments in stirred tanks and they found that the aggregation kernel decreases with increasing energy dissipation rate. Due to the enormous range of hydrodynamic environments in agitated systems, Mumtaz and Hounslow (2000) investigated the effect of hydrodynamics in Poiseulle flow. Mumtaz and Hounslow found that at low shear rates i.e. in the high efficiency regime, the aggregation rate constant, β_0, is small and varies linearly with shear rate, γ, providing good validation for Smoluchowski's theory. In addition, they found that at very high shear rates the aggregation rate decreases due to unsuccessful collisions and aggregate rupture confirming the disruptive role of fluid shear rate in impeding aggregation. This observation is shown graphically in Figure 2.14.

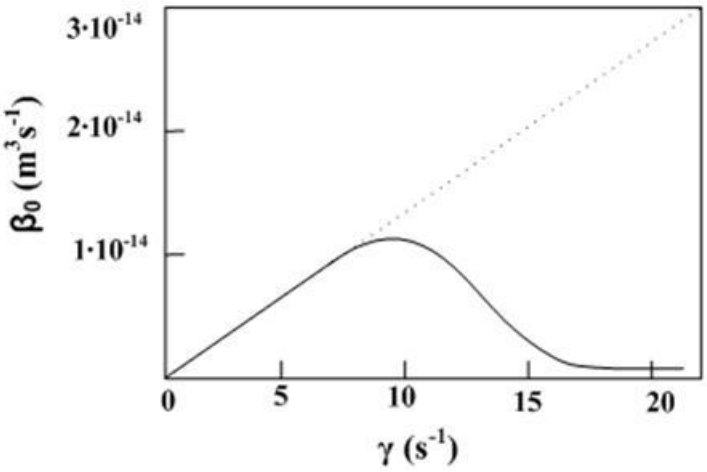

Figure 2.14 Aggregation kernel (β_0) vs. shear rate (γ) for calcium oxalate (adapted from Mumtaz and Hounslow, 2000).

Chapter 3. Experimental

3.1. Materials

All chemicals used in the preparation of the solutions ($CaCl_2$, $Na_2C_2O_4$, and CaC_2O_4) in this investigation were analytical grade Merck chemicals. The calcium ions were supplied by $CaC1_2$ and the oxalate ions by $Na_2C_2O_4$.

The solutions were made up to an ionic strength of 0.16 $kmol.m^{-3}$ by the addition of NaCl. The reasons for working at such high NaCl concentration are as follows:

a. The added salt makes the electric double layer at the crystal surface shrink. Particles do not have to overcome an energy barrier related to the double layers when approaching each other hence the only efficiency step of importance is the efficiency of a collision.
b. Na^+ and Cl^- are added as counter ions when the reactants are added to the suspension to create a supersaturation. These counter ions will influence all equilibria in the solution.

Adding such a large amount of background salt will result in the relative change in background ion concentration to be small but having a negligible influence on the solution chemistry (Hiemenz, 1986).

3.2. Apparatus

3.2.1. The oscillating grid reactor

The oscillating grid reactor is based on the oscillatory multi-grid mixer as used by Bache and Rasool (2001) and Changunda *et al.,* (2008). The oscillating multi-gird mixer was obtained from Changunda *et al*., who purchased it from Bache and Rasool. The experimental setup used in this study is shown in Figure 3.1.

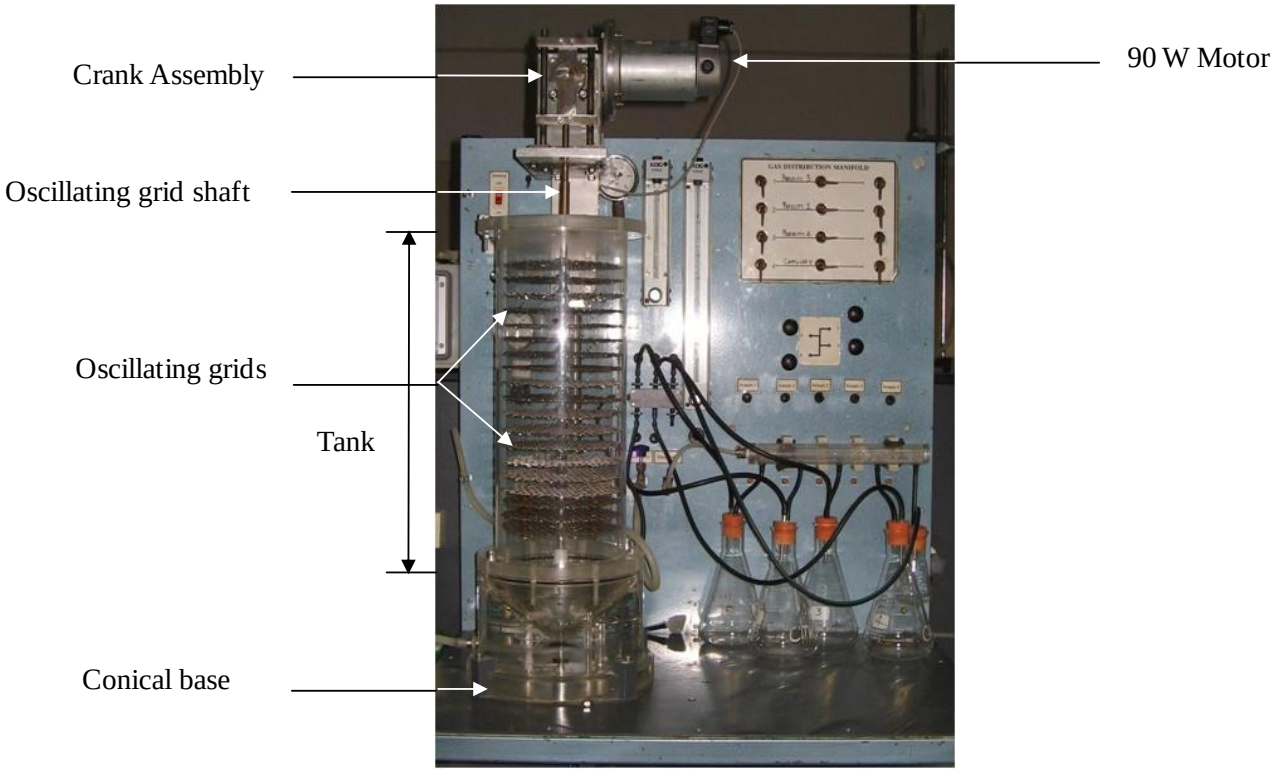

Figure 3.1 Experimental setup.

3.2.2. The reactor tank

The reactor tank consists of a cylindrical section and a right angled conical base held together with flanges. Figure 3.2 shows a schematic diagram of the two sections that make up the tank. The cylindrical section is 5 mm thick perspex because of its strength, transparency and easiness to clean. The conical base was constructed by combining 3 sheets of 30 mm thick Perspex then carefully creating a conical hole in it. This section is bolted down onto the stand for stability. The apex of the cone leads to a 10 mm cylindrical discharge hole for pump around and sampling.

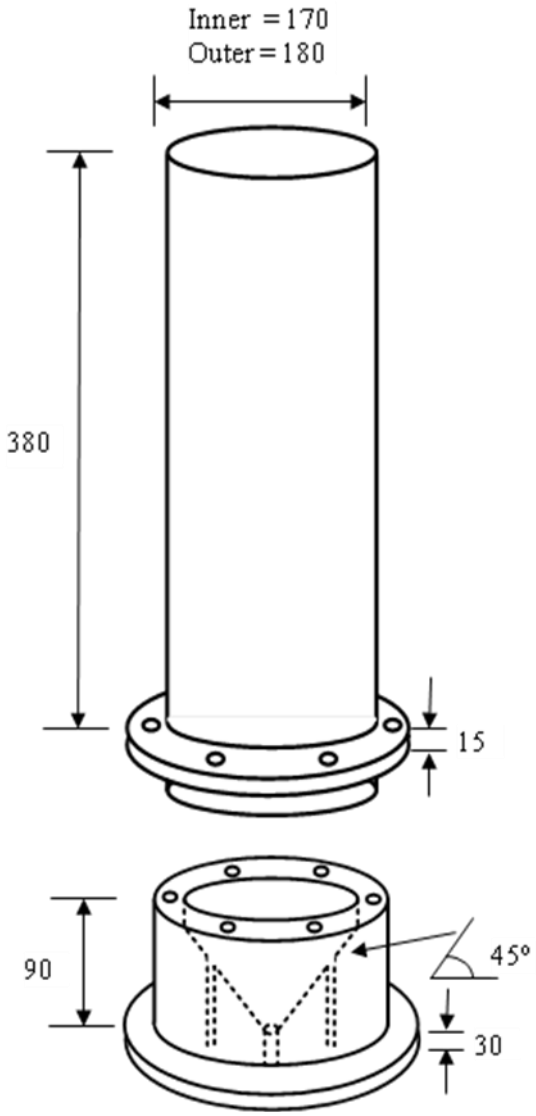

Figure 3.2 Schematic diagram of reactor tank.

3.2.3. Grid agitation system

The grid agitation system is illustrated in detail in Figure 3.3. The grids were formed from 1mm diameter stainless steel wire woven mesh with a hole size of 8 mm. The drive shaft assembly on which the grids were mounted was supported by PVC collar support at the conical base of the flotation column. The collar support had Teflon bearings to minimize friction. A 90 W motor with a perpendicular shaft gearbox crank assembly provided sinusoidal motion with a frequency up to 7.1 Hz. For the purposes of this study, the grids are oscillated at a fixed amplitude, equal to the grid spacing, and over the entire range of frequencies using a variable speed drive. The purpose of the oscillating grids in the rig was to induce a particular level of turbulence.

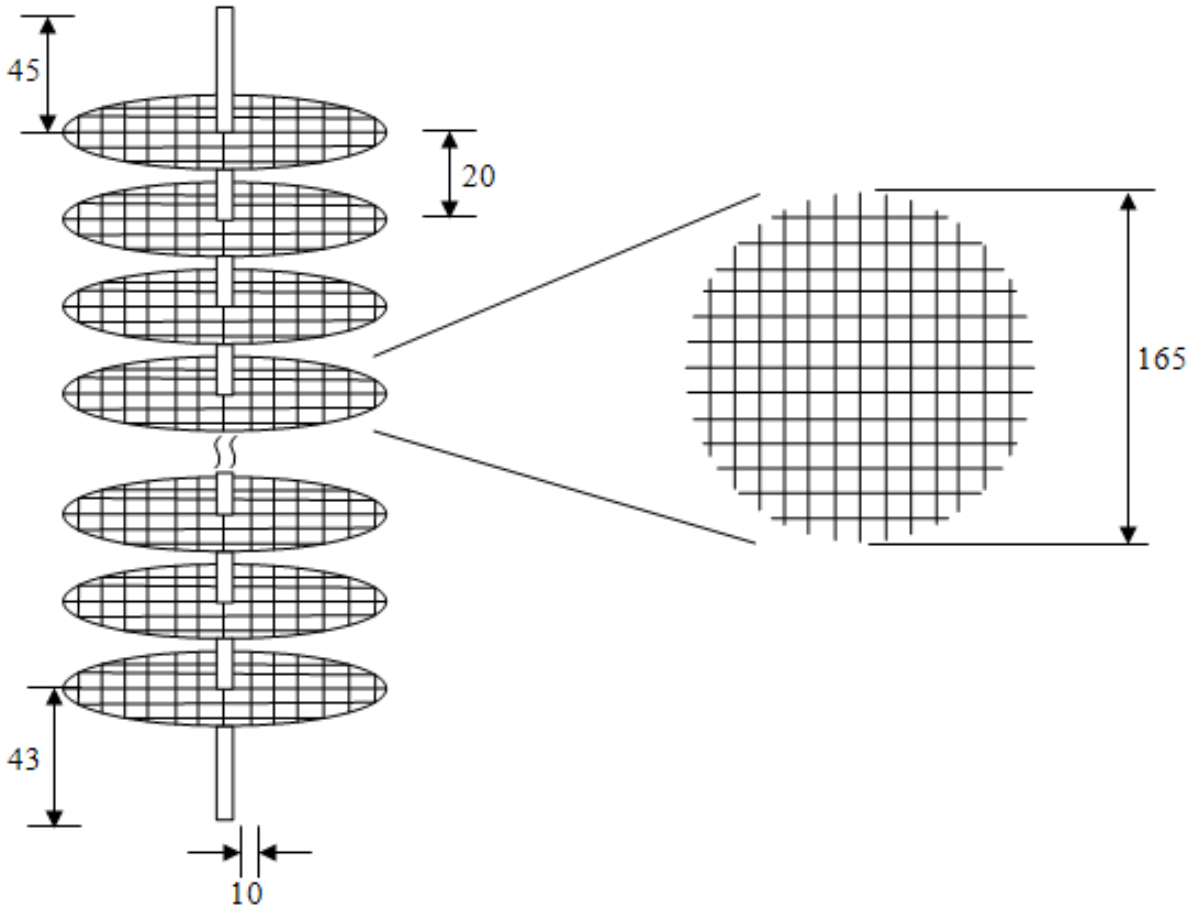

Figure 3.3 Grid agitation system.

3.2.4. Fluid flow distributor

A fluid flow distributor was added at the top of the reactor to allow for even distribution of flow into the reactor. It comprises a lid which has 2 inlets for the feed and the recycle and a reservoir which is 201cm^3 in volume, with 32, 2.5mm diameter inlet holes.

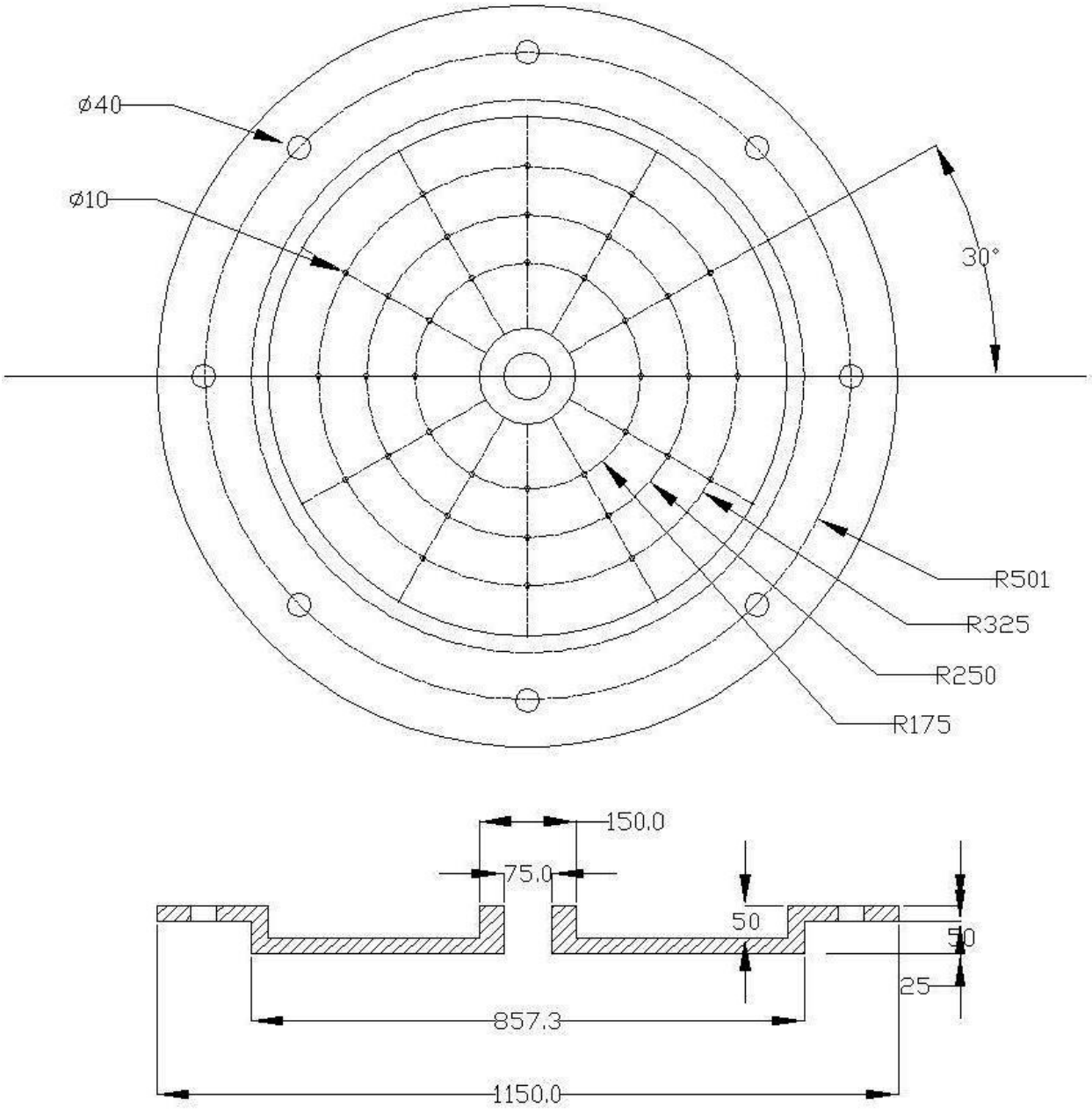

Figure 3.4 Distribution system (lid and reservoir).

3.3. Characterisation of the oscillating grid reactor

In this section, the oscillating grid reactor operating parameters as well as the gird specifications used in this study are highlighted. Table 3.1 shows the grids specifications of the reactor. These specifications include the grid stroke, bar diameter, grids solidarity and the coefficient associated with the variation in Reynolds number.

Table 3.1 Oscillating grids specification.

Grid stroke, S, (m)	0.0180
Bar diameter, d, (m)	0.00100
Grid solidarity,σ , (-)	0.220
Coefficient related to reynolds no. variation, α, (-)	0.350

Table 3.2 shows the oscillating grid reactor operating parameters. Five different energy input settings between 0.0 and 0.41 W/kg (or kW/m^3) were chosen. These correspond to grid frequencies of between 0 and 6 Hz, which are the operating limits of the oscillating grid reactor. The associated Reynolds numbers, power inputs of the grids as well as the energy dissipation rates are also shown in Table 3.2.

Table 3.2 Oscillating grid reactor operating parameters.

f (Hz)	R_N (-)	P_g (W)	ε (W/kg)
0	0	0	0
3.00	60.7	0.0310	0.0490
3.70	74.8	0.0550	0.100
5.10	103	0.135	0.250
6.00	121	0.212	0.410

3.4. Thermodynamics

Modelling was carried out using OLI® Stream Analyzer 2.0 for the batch experiments in order to deduce optimum operating conditions. OLI utilises a thermodynamic formulation to calculate Gibbs Free Energy, enthalpy, entropy, heat capacity and volume based on the calculation of the

standard state terms (G_o, H_o, S_o, Cp_o and V_o) using the framework of Helgeson and co-workers, and the frameworks of Bromley, Zemaitis, Pitzer and Debye-Huckel. From OLI® Stream Analyzer 2.0 several deductions were made on operating conditions:

1. The precipitation of calcium oxalate is not pH sensitive for 2<pH<12 (Refer to Figure 3.5).This resulted in the pH not being controlled however, the pH was monitored and recorded.
2. The precipitation of calcium oxalate can occur over a large temperature range (25 – 80°C) and as shown in Figure 3.6. Based on this result, experiments were carried out at 25 °C.

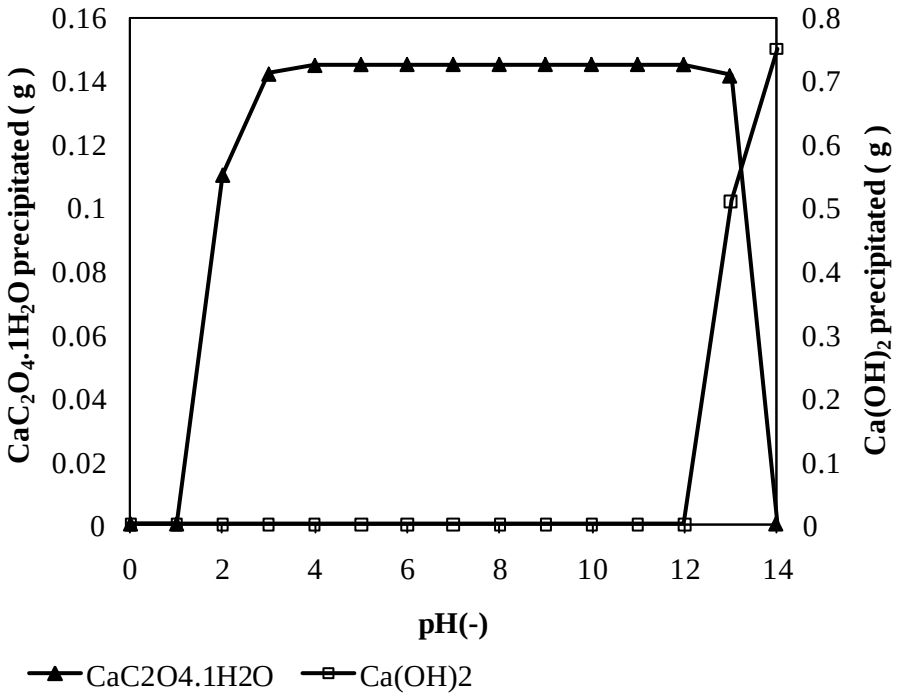

Figure 3.5 The effect of pH on the precipitation of calcium oxalate.

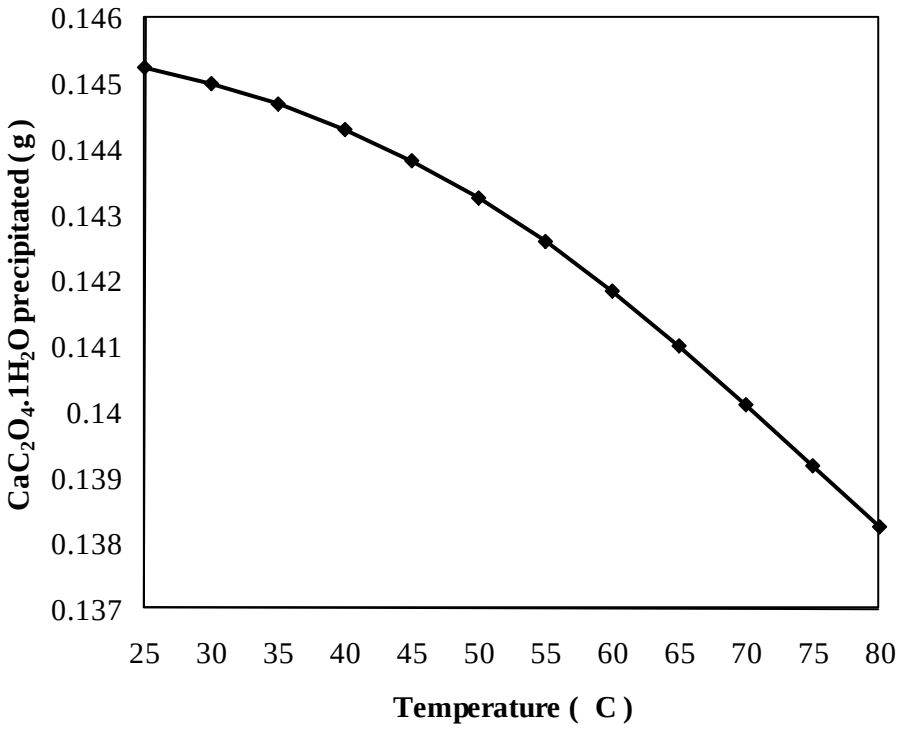

Figure 3.6 The effect of temperature on the precipitation of calcium oxalate.

3.5. Experimental programme

The reactor was first filled with 2.48 L of deionised water. The agitation grid system was switched and the frequency adjusted accordingly. A pump around recycle was switched on to assist in the suspension of the crystals. 0.01M $CaCl_2$ and 0.001 M $Na_2C_2O_4$, with both solutions having an ionic strength of 0.16 M, was pumped through a Y mixer using a Watson Marlow 505S pumps and into the reactor at a flow rate of 0.71 L/min. The reactor was filled up to 10 l. Samples were collected from the reactor and analysed. The laboratory room temperature was noted as well as the pH for every sample collected. All experiments were done in triplicate.

3.5.1. Sampling procedure and sample analyses

Samples were collected every 10 minutes from the bottom of the reactor using a syringe Methanol was immediately added to one part of the sample to quench the reaction and filtered through 0.20µm NY filter syringes. The filtrate was analysed for dissolved Ca^{2+} using Atomic absorption spectroscopy (AAS). The assay is only accurate to concentrations < 100 ppm therefore dilutions of samples were made. The other part of the sample was used to analyse the

particle size distribution (PSD) using the Malvern Mastersizer S. This apparatus utilises Mastersizer-S V2.19 software which uses light scattering. This technique is based around the principle that particles passing through a laser beam will scatter light at an angle that is directly related to their size. As the particle size decreases, the observed scattering angle increases logarithmically. The observed scattering intensity is also dependent on particle sizes and diminishes, to a good approximation, in relation to the particle's cross-sectional area.

At the end of each run (1hour), samples were collected and oven dried for 24 hours. A portion of these solids was used for X-ray diffraction (XRD). X-ray diffraction is a non-destructive analytical technique used to reveal the crystallographic structure and chemical composition of the material. The other portion was used for scanning electron microscope (SEM) to confirm the precipitated solid, the solid morphology and shape of particles. The SEM images the sample surface by scanning it with a high energy beam of electrons in a raster scan pattern. The electrons interact with the atoms that make up the sample producing signals that contain information about the sample's surface topography, composition and other properties such as electrical conductivity.

Chapter 4. Results and discussion

4.1. Repeatability studies

The experiments conducted in this study were carried out in triplicate. Figure 4.1 shows the repeatability results for the number based mean size, $L_{1,0}$, at time 20 minutes. Similar trends are observed for $L_{1,0}$ for all time intervals. The mean (x), the standard deviation (s) as well as the relative standard deviation (RSD %) are shown in Table 4.1.

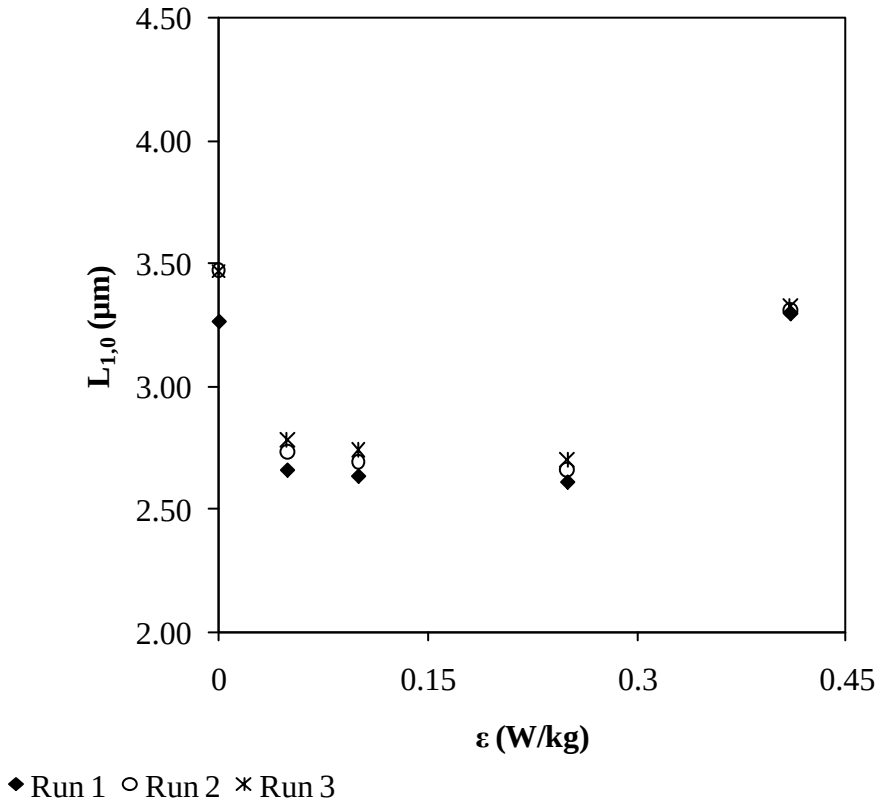

Figure 4.1 Variation of $L_{1,0}$ for repeatability studies.

Table 4.1 Variation of $L_{1,0}$ for repeatability experiments.

$L_{1,0}$			
ε (W/kg)	x	s	RSD %
0	3.40E-06	1.20E-07	3.53
0.0490	2.72E-06	6.33E-08	2.33
0.100	2.69E-06	5.52E-08	2.05
0.250	2.66E-06	4.87E-08	1.84
0.410	3.31E-06	1.62E-08	0.490

It is observed from Table 4.1 that the relative standard deviation for $L_{1,0}$ is less than 5 % for all cases. It can be concluded that the mean(s) drawn from these trends have a 95 % confidence. The relative standard deviation of the parameters shown in Figure 4.1 was used to compute the associated error with each experimental measurement.

4.2. Process characterisation

4.2.1. Process efficiency

Figure 4.2 shows the concentration profile of calcium ions remaining in solution with time for various energy inputs. In this study, process efficiency is characterised as the amount of calcium ions removed from solution as a function of time for different energy inputs.

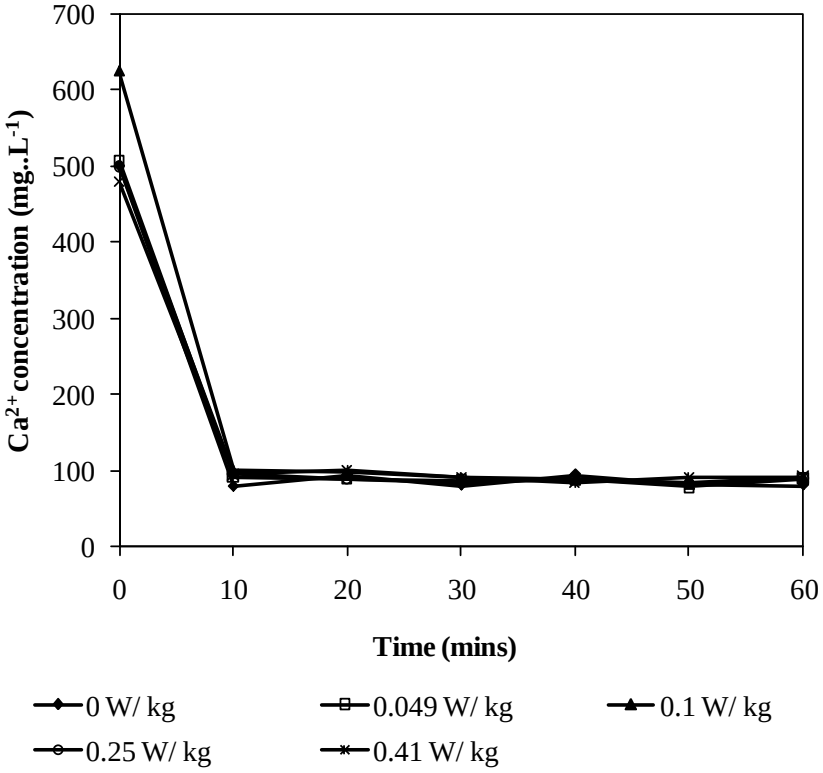

Figure 4.2 Concentration of Ca^{2+} remaining in solution.

Figure 4.2 shows that the concentration of Ca^{2+} decreases sharply from 500 ppm to 100 ppm in the first 10 minutes of the reaction, decreases slightly between 10 minutes and 20 minutes and remains constant thereafter. Figure 4.2 also indicates that most of the supersaturation is consumed during the first 20 minutes confirming that precipitation reactions occur at a fast rate. In addition, an increase in the concentration of Ca^{2+} is not observed, which indicates that no dissolution happens during the course of the reaction.

4.2.2. Precipitate characterisation

4.2.2.1. X-ray diffraction (XRD)

Figure 4.3 shows the X-ray diffraction spectra of the precipitated solid relative to the X-ray diffraction reference pattern of calcium oxalate monohydrate (vertical lines). From the analysis of the X-ray diffraction patterns, it can be seen that the spectra of the precipitated solid matches

with the reference pattern, confirming the precipitated solid is the stable hydrate, calcium oxalate monohydrate ($CaC_2O_4.1H_2O$). Figure 4.3 also indicates that no other polymorph is present.

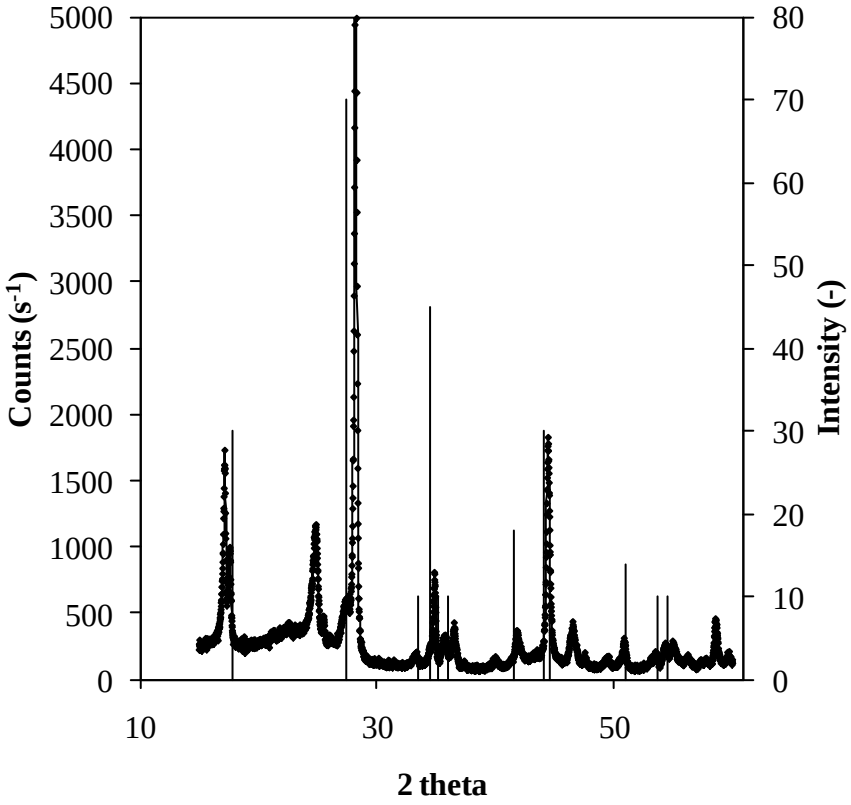

Figure 4.3 X-ray powder diffraction spectra of the precipitated solid.

4.2.2.2. Morphology

Figure 4.4 shows the SEM micrographs of the precipitates obtained at the end of each experiment for 0 W/kg and 0.41 W/kg respectively.

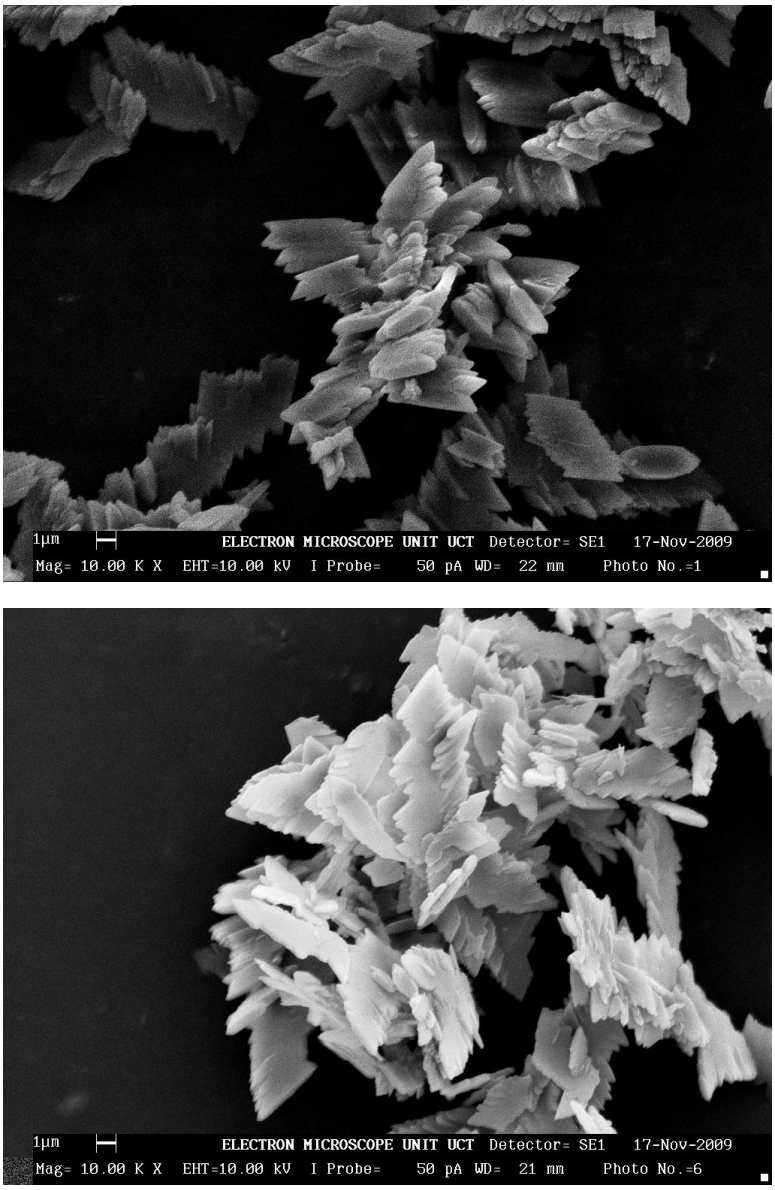

Figure 4.4 SEM micrographs of the precipitate formed for 0 W/kg and 0.41 W/kg.

Figure 4.4 shows that the precipitated calcium oxalate monohydrate crystals are flat, elongated jagged platelets. The SEM micrographs also show that the crystals precipitated in the typical monoclinic prismatic form. This observation was also reported by Houcine *et al*. (1997). In addition, the SEM micrographs show that the precipitate formed contains loosely associated crystallites. The crystals obtained for 0 W/kg portray a more defined crystallographic axis as compared to the crystals produced for the case of 0.41 W/kg. Possible mechanisms for the above observations will be discussed further in section 4.3.1.

4.2.2.3. Particle size distribution (PSD)

The typical particle size number distribution obtained in this study is shown in Figure 4.5. The distribution shown is for particles formed after 10 minutes of the reaction for different energy inputs. It should be noted that the height of the peaks can be related to the number of particles.

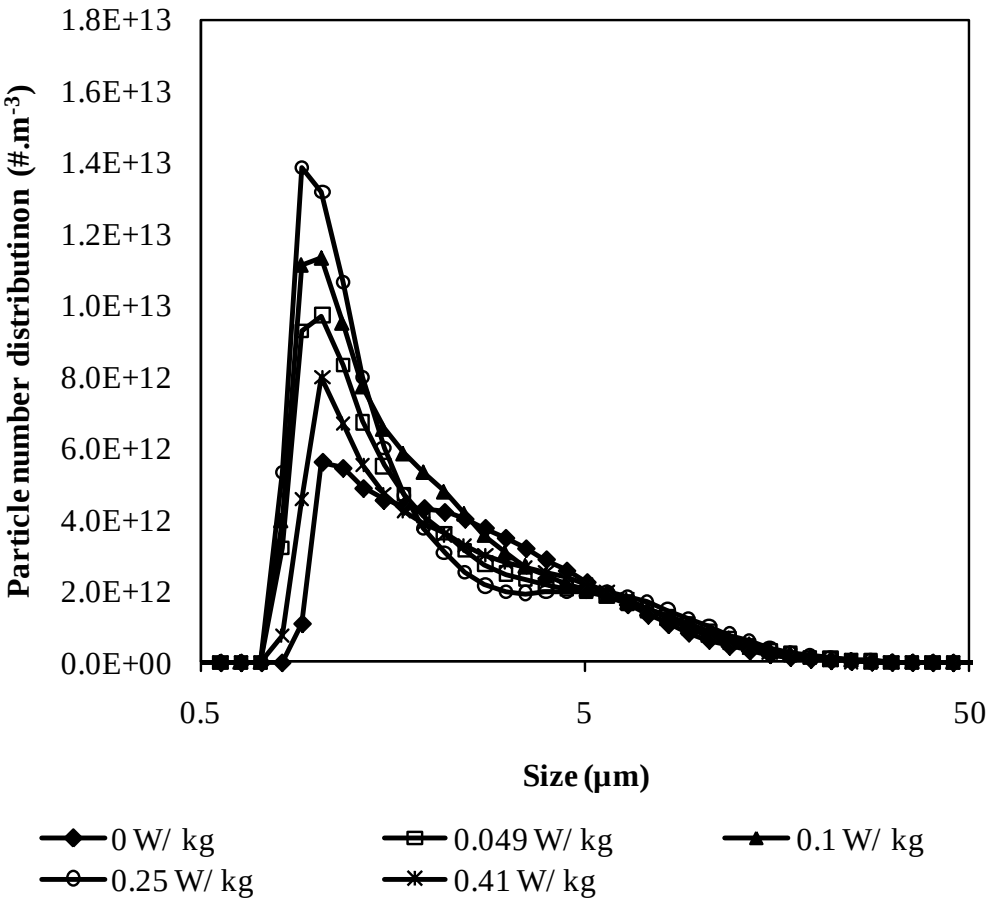

Figure 4.5 Particle size distribution.

The results show that for all energy inputs, a bimodal distribution is obtained. The number of particles increases with increasing energy input until 0.25 W/kg and then decreases. This increase in the number of particles indicates that there is an increase in the amount of precipitate formed in this time interval with an increase in energy input. Possible mechanisms and reasons to the above observations and evolution of the PSD's obtained are further discussed in section 4.3.2.

4.3. The effect of energy on crystallization

4.3.1. Particle morphology

Figure 4.6 shows the SEM micrographs of the precipitates obtained at the end each experiment for different energy inputs.

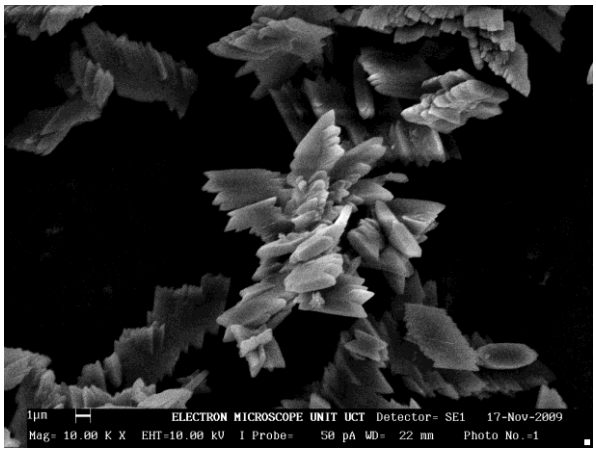

(a)

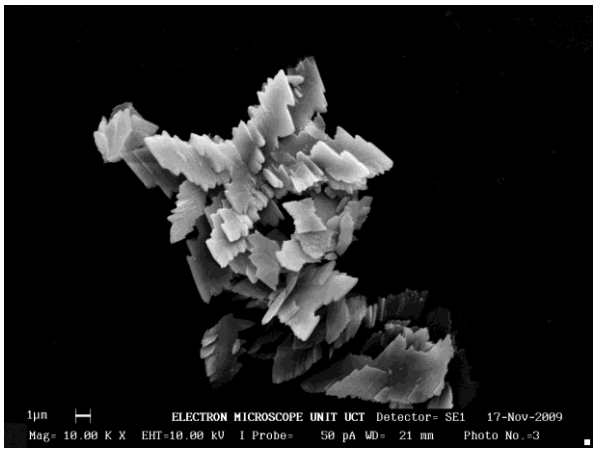

(b)

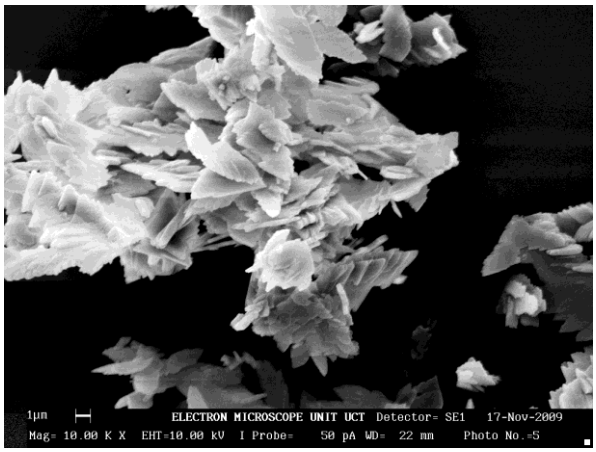

(c)

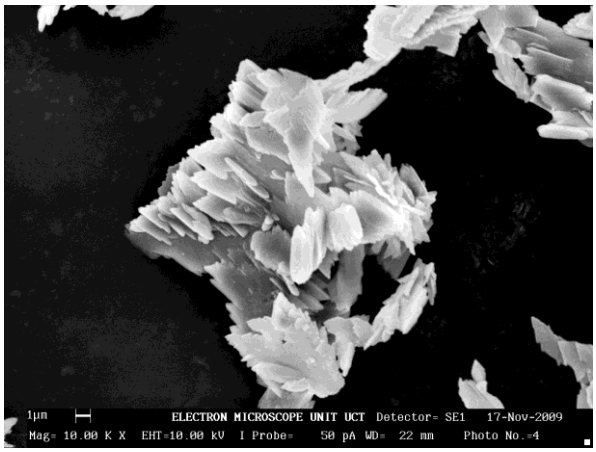

(d)

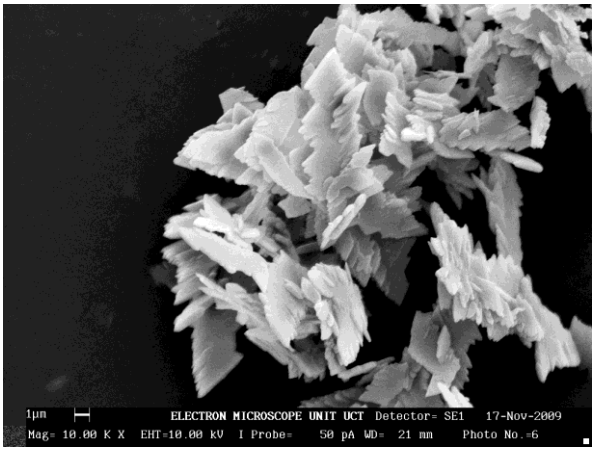

(e)

Figure 4.6 SEM micrographs of the precipitate formed for different energy inputs: (a) 0 W/ kg; (b) 0.049W/ kg; (c) 0.1 W/ kg; (d) 0.25 W/ kg; (e) 0.41 W/ kg

Crystals with clear crystallographic axis are obtained at low energy inputs (Figure 4.6 a, b) but this symmetry becomes less apparent with increasing energy input (Figure 4.6 c, d, e). The crystallographic axis observed at the low energy inputs (0 – 0.049 W/kg) is indicative of crystal growth since crystal growth is characteristic of solute molecules depositing into the crystal face and then the crystal face growing outwards. At high energy inputs (0.1 – 0.41 W/kg), the less apparent symmetry of the crystals is indicative of aggregation. This is because particle size enlargement by aggregation is dominated by particle collisions, which are affected by the hydrodynamics of the system.

4.3.2. Particle size distribution (PSD)

Figure 4.7 shows the particle number distribution, N ($\#.m^{-3}$), for energy inputs ranging from 0.1 – 0.41 W/kg after 10 minutes and 60 minutes of the reaction.

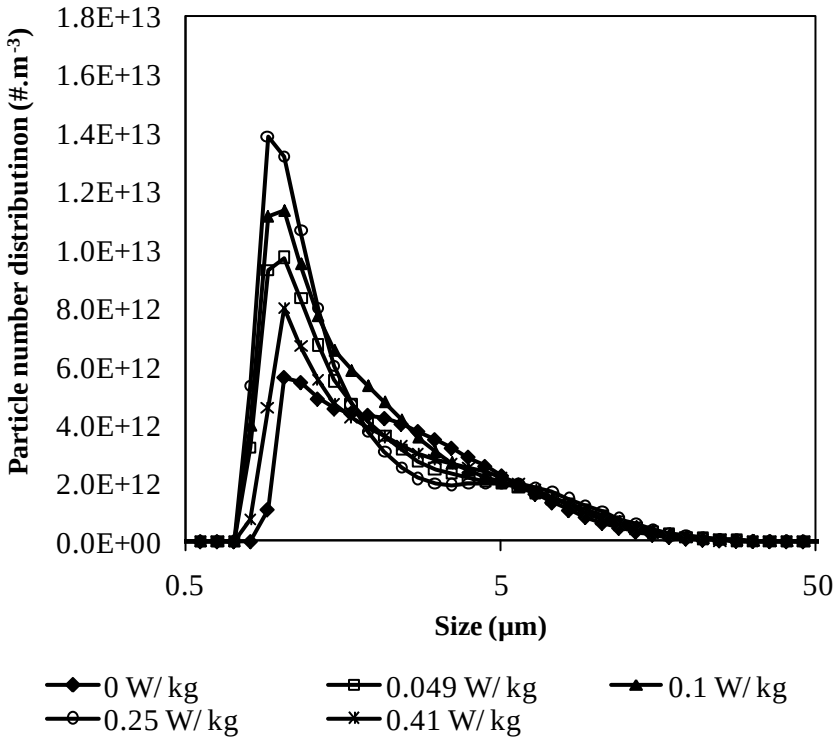

(a)

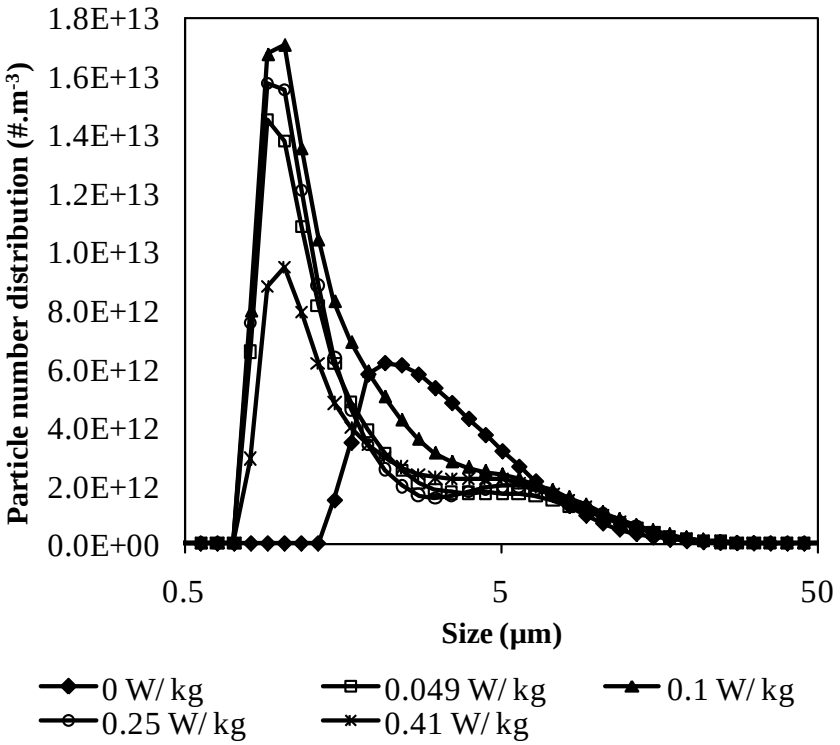

(b)

Figure 4.7 Evolution of PSD for different energy inputs: (a) 10 minutes and (b) 60 minutes.

Similar trends are observed in the evolution of the PSDs for all time intervals, suggesting that the active particle rate processes are similar in all cases. The particle size distributions (PSD) are bi-modal, indicating that the system contains poly-dispersed particles. This bimodal shape suggests the presence of aggregates and it is confirmed by the SEM photographs which show the presence of aggregation as the agitation rate is increased. In literature, (Bramley *et al*., 1996 and Hounslow *et al*., 2001), the particle size distribution obtained for the calcium oxalate system is mono-modal. This is because most authors conduct their studies using seeded a system which controls supersaturation and suppresses nucleation.

It is observed that for 0 W/kg, the number of particles decreases slightly with time, with an increase in modal size. However, for energy inputs between 0.049 W/kg and 0.41 W/kg, the number of particles increases with time with no change in the modal size. The increase in the number of particles in the reactor could be due to either nucleation and (or) attrition. Aggregation results in an increase in particle size and decrease in the number of particles whereas growth results in an increase in the mean size with no change in the number of particles. For the case of 0 W/kg, the modal size increases from 1.03 to 2.150μm. This increase in modal size and slight decrease in the number of particles in the reactor (hence larger particles) could be a result of aggregation and high crystal growth rates because of localised supersaturation.

Figure 4.7 also shows that the number of particles increases with specific energy input from 0 – 0.25W/kg and then decreases for 0.41 W/ kg at time 10 minutes. However, at 60 minutes the number of particles increases with specific energy input from 0 – 0.1W/kg and then decreases. This increase in the number of smaller particles is most likely due to the nucleation. An increase in energy input has been observed to promote nucleation (Zauner and Jones, 2000). The decrease in the number of particles could be as a result of either aggregation or dissolution. Figure 4.2 shows that there is no increase in the concentration of calcium ions in solution with time, providing evidence that the decrease in the number of particles was not due to dissolution but rather due to aggregation becoming the dominant process.

Based on the mass deposition rates and assuming particles are spherical, the maximum particle size that could be achieved by molecular growth alone, d_{max}, can be calculated from equation 4-1 (Söhnel and Mullin, 1991).

$$d_{max} = 2\left(\frac{3V_m\Delta c}{4\Pi N_0}\right)^{1/3} \qquad 4\text{-}1$$

Where

V_m: solid molar volume ($m^3.mol^{-1}$)

Δc: concentration driving force, based on total mass deposited ($mol.m^{-3}$)

N_0: number of particles present per unit volume ($\#.m^{-3}$)

The maximum particle size that could be achieved by molecular growth is 1.138µm, thus it is unlikely that the particles at the 10 and 40µm modal sizes were formed by molecular growth alone, suggesting that aggregation played a major role in the formation of these particles.

4.3.3. Number based mean

The PSD data was transformed into moments and these moments were used to obtain the particle size evolution with time. The evolution of number based mean, $L_{1,0}$, is shown graphically in Figure 4.8.

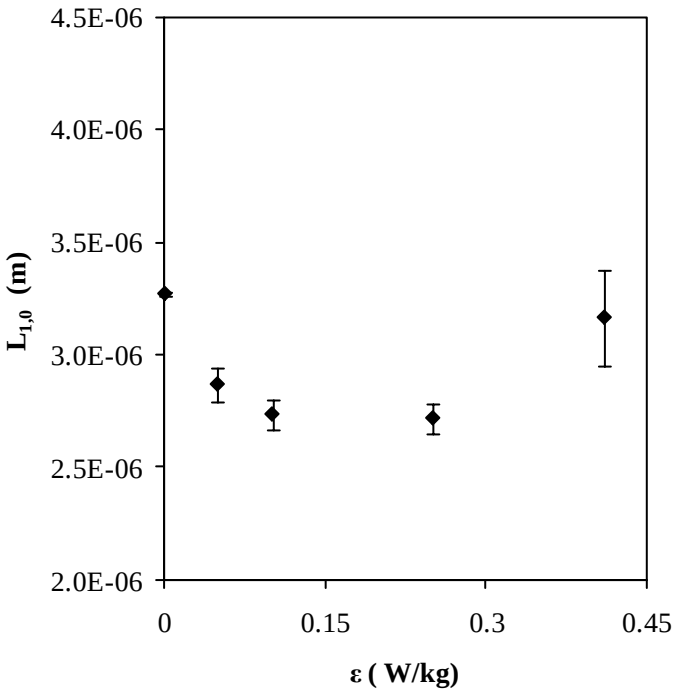

(a)

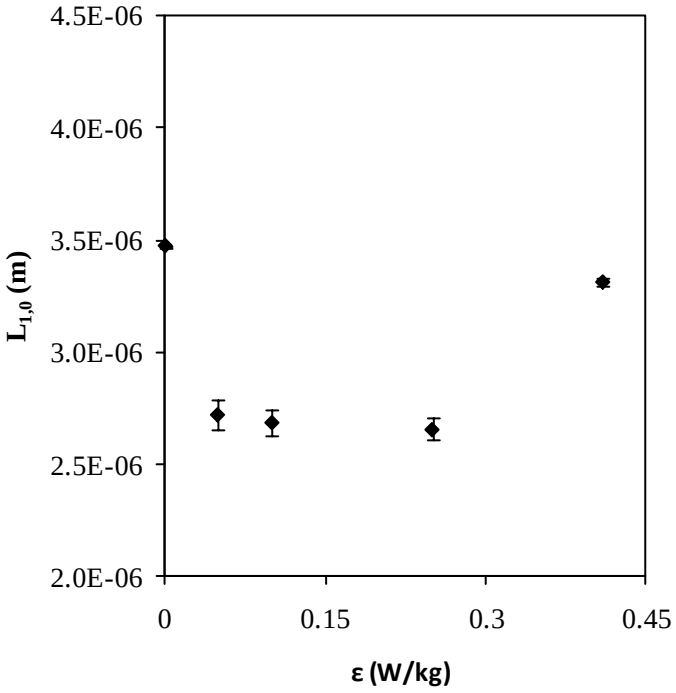

(b)

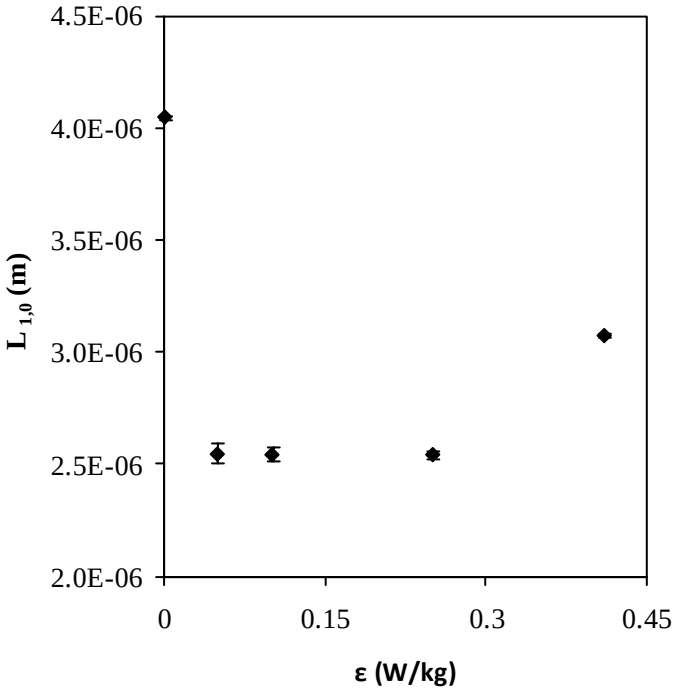

(c)

Figure 4.8 Evolution of number based mean ($L_{1,0}$) at various time intervals: (a) 10 minutes, (b) 20 minutes and (c) 60 minutes.

Figure 4.8 shows that the $L_{1,0}$ increases with time when there is no agitation and decreases with time when there is agitation. This increase in particle size supports the assumption of high growth rates occurring and formation of primary agglomerates when there is no agitation. This observation has also been reported by Zauner and Jones (2000).

The trend for the evolution of $L_{1,0}$ as a function of energy input decreases for $0 < \varepsilon < 0.1$ W/kg and reaches a minimum at 0.1 W/kg. It then remains constant between 0.1 W/kg and 0.25 W/kg and increases for $\varepsilon > 0.25$ W/kg for all time intervals. The observed trend in Figure 4.8 is in agreement with the particle size distribution (Figure 4.7) which showed an increase in the number of smaller particles with an increase in energy. It is most likely that nucleation is the dominant process for energy inputs less than 0.1 W/kg. The SEM micrographs showed that the precipitate formed contains loosely associated crystallites therefore a small injection of energy into the system can result in these particles to be dispersed providing surfaces for secondary nucleation (fluid shear breeding- refer to section 2.3.3.1). This type of nucleation has been observed by authors such as Powers (1963) (as cited by Mullin, 2001) who conducted experiments on sucrose and Gyulai (1948) (as cited by Mullin, 2001) who conducted experiments on potassium bromide. For energy inputs between 0.1 W/kg and 0.25 W/kg where there is no change in the particle size could be an indication that the rate of formation of nuclei is the same as the rate of aggregation. For energy inputs greater than 0.25 W/kg, the size enlargement process (aggregation) becomes the dominant process. This trend was not expected because an increase in the rate of energy dissipation of fluid enhances crystal-crystal collisions and the expected result is an increase in aggregation which leads to an increase in the particle size.

It must be taken into consideration that the number based mean, $L_{1,0}$, is influenced more by large numbers of small particles, which is the case in this research. Hence the number based mean, $L_{1,0}$, is more representative of the behaviour of the smaller particles within the system. The initial decrease in $L_{1,0}$ is a clear indication than an increase in energy input promotes secondary nucleation. The weight equivalent mean, $D_{4,3}$, is measured based on a volume distribution, volume/mass hence it would be the most significant mean to use to convey information about the

larger particles of the PSD. Analysis of this parameter together with the number based mean will give a clear indication of the effect of energy input on the system as a whole.

4.3.4. Weight equivalent mean

The evolution of the weight equivalent mean, $D_{4,3}$, as a function of energy input is shown in Figure 4.9.

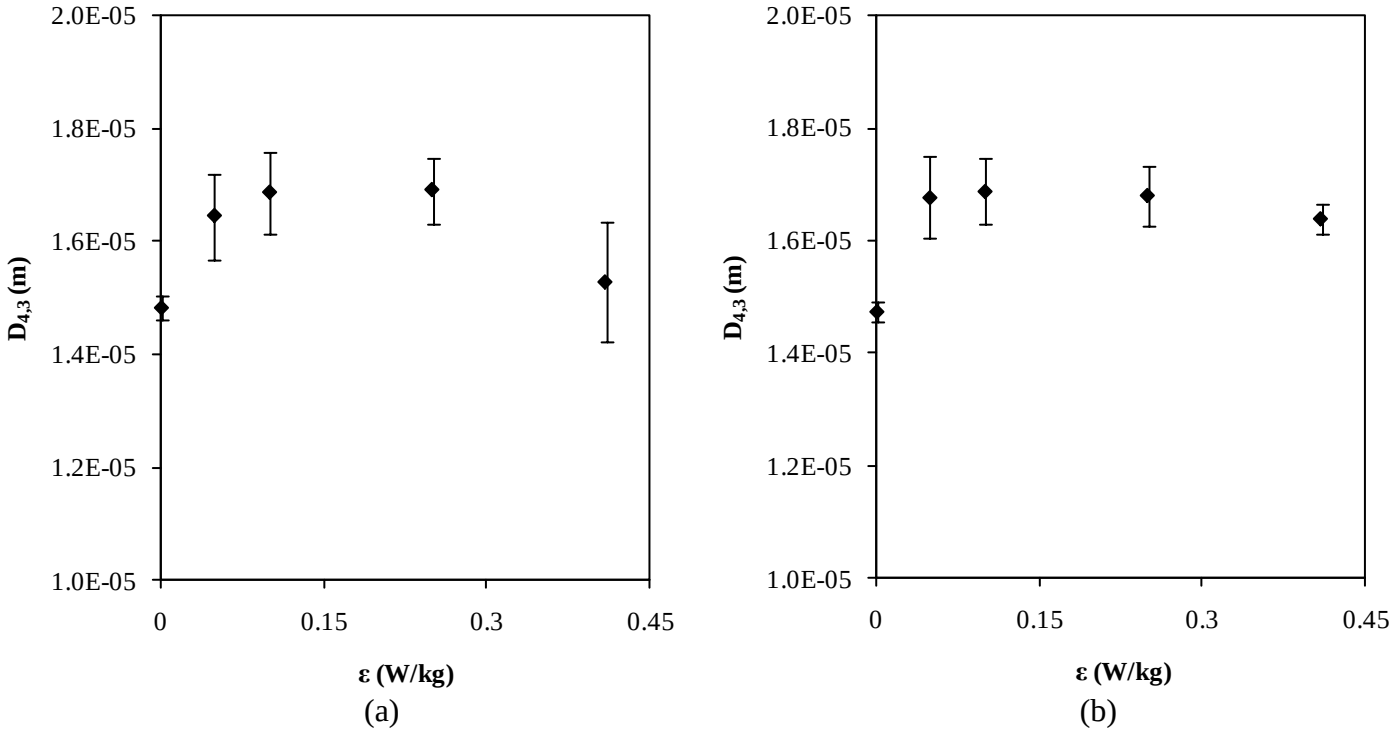

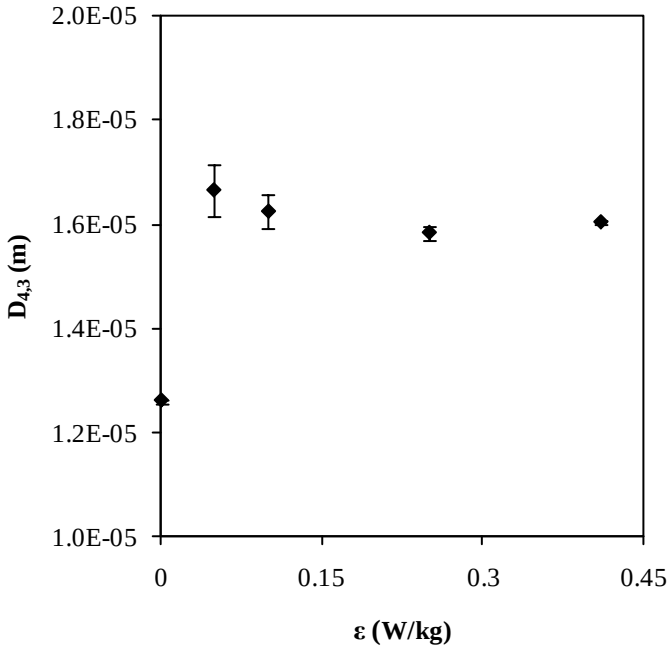

(c)

Figure 4.9 Evolution of weight equivalent mean ($D_{4,3}$) at various time intervals: (a) 10 minutes, (b) 20 minutes and (c) 60 minutes.

An increase in the weight equivalent mean is noted for energy inputs less than 0.1 W/kg. As the energy input increases, above 0.1 W/kg, a decrease is observed. This trend is less defined at time 60 minutes where after 0.1 W/kg, the mean size decreases slightly at 0.25 W/kg and thereafter remains constant.

Since aggregation and growth results in an increase in the mean size and nucleation and breakage results in a decrease in the mean size, the active rate processes occurring on the bigger particles can be identified from the evolution of $D_{4,3}$. The increase in the weight equivalent mean could be due to aggregation and (or) growth however, this particle size enlargement could not only be attributed to growth alone because the maximum particle size achieved by molecular growth alone for this system is 1.138μm. This implies that aggregation played a role in the enlargement of these particles. The decrease in the mean size could be due to breakage and a decrease in aggregation efficiency becoming apparent at higher energy dissipation rates. The unchanging particle size for time 60 minutes from 0.25 W/kg could be an indication that attrition and

aggregation have reached a dynamic equilibrium where, the rate of aggregation is the same as the rate of particle breakage.

Overall, the observed trend for the weight equivalent mean as a function of energy input reaching a maximum, and then decreasing was expected. An increase in energy dissipation of fluid enhances crystal-crystal collision (Kruis and Kuster, 1997; Staffman and turner, 1956; Delichatsois and Probstein, 1974) resulting in an increase in aggregation therefore, an increase in the particle size. However, higher fluid shear rates also result in larger hydrodynamic forces and shorter time scales for bridge formation. Hence there are larger stresses in the bridge formation between particles resulting in unsuccessful collisions (decrease in aggregation efficiency) and aggregate breakage/rupture resulting in a decrease in particle size. This phenomenon has also been observed by various authors such as Bramley and co-workers (1996) as well as Mumtaz and Hounslow (2000).

4.3.5. Aggregation kernel

In this study, a size-independent aggregation model that uses the equations of moments is used to determine the extent of aggregation. Bramley and co-workers (1996) showed that the size-independent kernel is the most appropriate kernel for the aggregation of calcium oxalate monohydrate (COM) as compared with other models. Figure 4.10 shows the effect of agitation on the aggregation kernel.

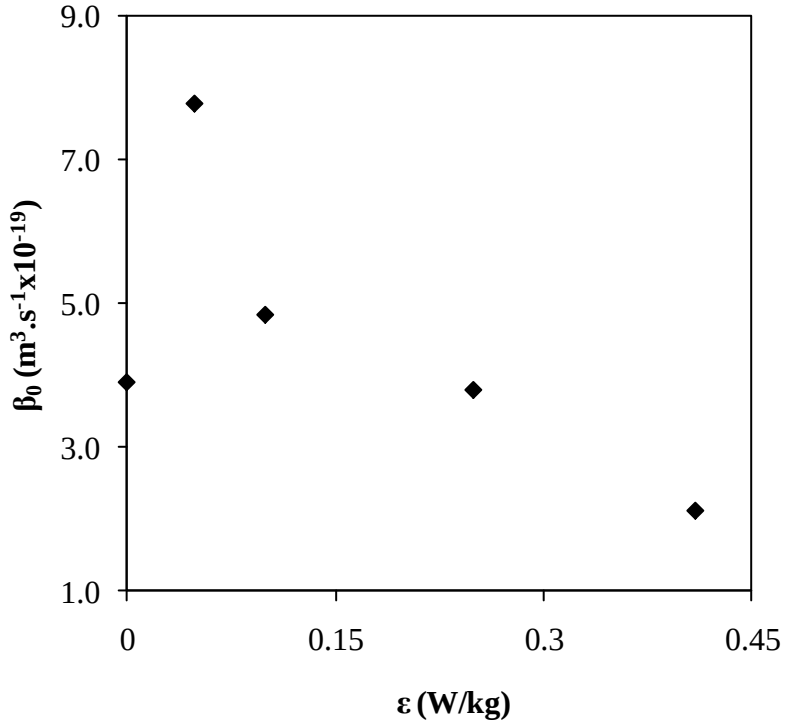

Figure 4.10 Aggregation kernel vs. energy dissipation.

The size independent aggregation kernel starts at $3.9x10^{-19}$ $m^3.s^{-1}$, abruptly increases to $7.79x10^{-19}$ $m^3.s^{-1}$ at 0.049W/kg and gradually decreases afterwards. However, this trend is different to what is observed in literature. The trend observed in literature is a gradual increase in the aggregation kernel followed by a gradual decrease (concave up, concave down – see Figure 2.14). An explanation for this observation could be that in this study, aggregation is not the only process occurring during the course of the experiment. Nucleation, aggregation, growth and breakage are all occurring simultaneously and the net effect of all these mechanisms is propagated in the kernel. The exhibited maximum in the size independent kernel with increasing power input suggesting a decrease in aggregation efficiency and breakage at higher energy inputs resulting in a deviation from Smoluchowski's theory is consistent with findings of Mumtaz *et al.* (1997), Mumtaz and Hounslow (2000) and Zauner and Jones (2000).

Table 4.2 shows β_0 values found in this study as well as in literature. It is observed that the β_0 values found in this study are lower than those found by the various authors in literature. The

reason for the lower values could be that most authors who conducted similar experiments such as Mumtaz and Hounslow (2000) as well as Bramley and co-workers (1996) conducted experiments using seeded systems where supersaturation is controlled and nucleation suppressed. In this study on the other hand, seeding was not used.

Table 4.2 Size independent aggregation kernel values.

Current study findings (2010)	**3.90×10^{-19} - 2.10×10^{-19}**
Hounslow and co-workers (2001)	1.00×10^{-14} - 3.00×10^{-14}
Mumtaz and Hounslow (2000)	1.00×10^{-14} - 3.00×10^{-14}
Bramley and co-workers (1996)	8.00×10^{-15} - 3.20×10^{-14}

From the above results, the kernel obtained in this study should be redefined as the "overall kernel" or "effective kernel" rather than the aggregation kernel because all four rate processes (nucleation, growth, aggregation and breakage) are embedded in the results.

4.3.6. Growth and nucleation rates

Although the focus of this project was to investigate the effect of energy input on aggregation, nucleation and growth rates were also calculated for this system to compare with literature and to broaden the understanding of other mechanisms taking place.

The nucleation rate was calculated by assuming that there is no breakage, thus the nucleation rate was obtained by dividing m_0 by time. These values are at best approximate estimates because the effects of breakage have been neglected. The Nucleation rates ranged from 3.10×10^{10} to 8.18×10^{10} $m^{-3}s^{-1}$ and are within the nucleation rates calculated for the calcium oxalate system found in literature (5.6×10^{8} to 2.8×10^{11} $m^{-3}s^{-1}$). The values obtained in this study are higher than those observed by Garside and co-workers (1982) who operated at the same feed concentrations, however, at a higher temperature of 37°C.

The growth rates were calculated using the moment form of the population balance described by equation 2-40. The calculated rates for calcium oxalate obtained are in the range of 1.35×10^{-9} to $4.14 \times 10^{-9} m.s^{-1}$. In literature, growth rates vary considerably: $1.08 \times 10^{-8} m.s^{-1}$ (Kavanagh, 1992),

$5.0x10^{-8}$ to $3.4x10^{-9}$ $m.s^{-1}$ (Garside *et al*., 1982) and $1.11x10^{-10}$ to $2.8x10^{-10}$ $m.s^{-1}$ (Nielsen and Toft, 1984). The values obtained from the experiments are also within the range of the literature data.

4.4. Summary of findings

From the results presented in this section, the following key findings can be identified:

- Precipitation of calcium oxalate monohydrate is a fast process, with most of the supersaturation being consumed in the first 20 minutes of the reaction;

- The crystals precipitate out in the typical monoclinic prismatic shape appearing as flat elongated jagged platelets. At low energy inputs, the crystals have a more defined crystallographic axis as compared to crystals produced at high energy inputs. This indicates that at low energy inputs growth is a more dominant process whereas aggregation becomes more apparent at higher energy inputs;

- The trend for the number based mean shows that at low energy inputs, there is a decrease in the $L_{1,0}$ ($0 < \varepsilon < 0.1$) and at higher energy input ($\varepsilon > 0.1$ W/kg), the number based mean increases. This decrease in $L_{1,0}$ indicates the presence of smaller particles which is due to nucleation whereas the increase in the $L_{1,0}$ is due to aggregation.

- The weight equivalent mean increases as energy input increases, reaching a maximum at 0.1 W/kg and then decreases. This increase in the $D_{4,3}$ could be due to aggregation and (or) growth. The decrease in the mean size at higher energy dissipation rates could be due to breakage and a decrease in aggregation efficiency;

- A maximum is exhibited in the size independent kernel at 0.049 W/kg, suggesting a decrease in aggregation efficiency and breakage at higher energy inputs.

Chapter 5. Conclusions and recommendations

This study investigated the effect of energy input on the precipitation kinetics of calcium oxalate monohydrate (in particular aggregation). The objective of the study was to gain an understanding of the precipitation kinetics in a nearly homogeneous isotropic turbulent environment and to achieve the set objective, experiments were carried out in an oscillating multi-grid reactor run in batch mode.

5.1. Conclusions

From the results presented in this work, the following conclusions can be drawn:

- All four particle formation mechanisms, nucleation, growth, aggregation and breakage, were active in the precipitation of calcium oxalate, producing the typical monoclinic prismatic calcium oxalate monohydrate crystals;

- The evolution of the number based mean, $L_{1,0}$, which conveys information about the smaller particles of the PSD, shows that an increase in energy input promotes nucleation for $\varepsilon < 0.1$ W/kg however, at $\varepsilon > 0.1$ W/kg, aggregation becomes the dominant rate process;

- The evolution of the mass based mean, $D_{4,3}$, which conveys information about the larger particles of the PSD, shows that an increase in energy input promotes aggregation ($\varepsilon < 0.1$ W/kg), however at $\varepsilon > 0.1$ W/kg, aggregation inefficiency and aggregate breakage becomes the dominant rate processes;

- Results from the investigation of the effect of energy input on the aggregation kernel exhibited a maximum in the size independent aggregation kernel at 0.049 W/kg, suggesting a decrease in aggregation efficiency and breakage at

higher energy inputs. This trend shows the disruptive role of hydrodynamics on aggregation.

5.2. Recommendations

Based on the above conclusions, it is recommended that various aspects of precipitation using the oscillating multi-grid mixer are further investigated:

Process conditions

1. In this project, the focus was only on the effect of energy input on aggregation. Other process conditions need be looked into i.e.: the effect of supersaturation and the effect of temperature. In this way other variables can be looked at in depth, such as the growth rate of Calcium oxalate and the effect of process conditions.

Modelling techniques

2. Other modelling techniques should be considered and evaluated. The use of computational fluid dynamics (CFD) modelling can help in attaining solid volume fraction, heat transfer and temperature profiles when investigating the effect of temperature. It can also aid in the development of reactor compartmental modelling framework to facilitate modelling and eventual scale-up and design.

Reactor Configuration

3. The same experiments should be conducted in other reactor configurations (e.g. a stirred tank reactor, plug flow reactor, fluidised bed reactor). This will result in a direct comparison of the influence of hydrodynamics using experimental findings in addition to those obtained in literature.

Sampling Techniques

4. SEM and XRD samples should be taken periodically during the course of the reaction rather than only at the end of each experiment to gain a more detailed understanding of morphology and crystal habit with time.

References

Armenante, P. M., Atiemo-Obeng, V. and Penny, W. R., 2006. Multiphase mixing and solid-liquid mixing in agitated reactors. Encyclopedia of Chemical Processing, Taylor and Francis.

Andreassen, J. P., 2004. Formation mechanism and morphology in precipitation of vaterite - nano - aggregation or crystal growth. Journal of Crystal Growth, 274: 256-264.

Andreassen, J. P. and Hounslow, M. J., 2004. Growth and aggregation of vaterite in seeded batch experiments. American Institute of Chemical Engineering Journal, 50: 2722-2782.

Appa, H. and Deglon, D. A., 2007. Multiphase CFD modelling of stirred tanks. Cape Town, University of Cape Town, MSc Engineering.

Ayazi-Shamlou, P. and Tichener-Hooker, N., 1993. Turbulent aggregation and break-up of particles in liquids in stirred vessels. Butterworth Heinemann, London.

Bache, D. H. and Rasool, E., 1996. Measurement of the energy dissipation around an oscillating grid by an energy balance approach. Chemical Engineering Journal, 63: 105-115.

Bache, D. H. and Rasool, E., 2001. Characteristics of turbulence in a multi-grid mixer. Chemical Engineering Journal, 83: 67-68.

Baldyga, J. and Bourne, J. R., 1999. Turbulent mixing and chemical reactions. John Wiley and Sons, Chichester.

Batchelor, G. K., 1970. An introduction to fluid dynamics. Cambridge University Press, Cambridge.

Bramley, A. S., Hounslow, M. J. and Ryall, R. L., 1996. Aggregation during precipitation from solution: a method of extracting rates from experimental data. Journal of Colloid and Interface Science, 183: 155-165.

Bramley, A. S., Hounslow, M. J. and Ryall, R. L., 1997. Aggregation during precipitation from solution. Kinetics for calcium oxalate monohydrate. Chemical Engineering Science, 52: 747-757.

Bramley, A. S., Hounslow, M. J., Newman, R., Paterson, W. R. and Pogessi, C., 1997. The role of solution composition on aggregation during precipitation. Institution of Chemical Engineers, 75:119-124.

Brown C. M., Ackermann, D. K., Purich, D. L. and Finlayson, B., 1991. Nucleation of calcium oxalate monohydrate: Use of turbidity measurements and computer-assisted simulations in characterising early events in crystal formation. Journal of Crystal Growth, 108: 455-464.

Brunk, B. K., Koch, D. L. and Lion, L., 1998. Observations of coagulation in isotropic turbulence. Journal of Fluid Mechanics, 371: 81-107.

Collier, A. P. and Hounslow, M. J., 1999. Growth and aggregation rates for calcite and calcium oxalate monohydrate. American Institute of Chemical Engineering Journal, 45: 2298-2305.

Delichatsios, M. A. and Probstein, R. F., 1974. Coagulation in turbulent flow: theory and experiment. Journal of Colloid and Interface Science, 51:394-404.

Eidelman, A., Elperin, T., Kleeorin, N., Markovich, A. and Rogachevskii, I., 2002. Oscillating grids turbulence generator for turbulent transport studies. Nonlinear Processes in Geophysics, 9: 201-205.

Eidelman, A., Elperin, T., Kleeorin, N., Markovich, A. and Rogachevskii, I., 2006. Experimental detection of turbulent thermal diffusion of aerosols in non-isothermal flows. Nonlinear Processes in Geophysics, 13: 109-117.

Garside, J., Brečević, L. J. and Mullin, J. W., 1982. The effect of temperature on the precipitation of calcium oxalate. Journal of Crystal Growth, 57:233-240.

Garside, J. and Tavare, N. S., 1985. Mixing, reaction, and precipitation limits of micromixing in an MSMPR crystallizer. Chemical Engineering Science, 40: 1485-1493.

Gradl, J., Schwarzer, H., Schwertfirm, F., Manhart, M. I. and Peukert, W., 2006. Precipitation of nano particles in a T-mixer: coupling the particle population dynamics with hydrodynamics through direct numerical simulation. Chemical Engineering Processing, 45: 908-916.

Hartel, R. W., Gottung, B. E., Randolph, A. D. and Drach, G. W., 1986. Mechanisms and kinetic modelling of calcium oxalate crystal aggregation in urine-like liquor. Part1. American Institute of Chemical Engineering Journal, 32: 1176-1185.

Hiemenz, P. C., 1986. Principles of colloid and surface chemistry. Marcel Dekker Inc., New York.

Hollander, E., 2002. Shear induced agglomeration and mixing. Netherlands: Delft University, PhD.

Hopfinger, E. J. and Toly, J. A., 1976. Spatially decaying turbulence and its relation to mixing across density interfaces. Journal of Fluid Mechanics, 78: 155-175.

Houcine, I., Plasari, E., David, R. and Villermaux, J., 1997. Influence of mixing characteristics on the quality and size of precipitated calcium oxalate in a pilot scale reactor. Transactions of the Institute of Chemical Engineers, 75: 252-256.

Hounslow, M. J., Ryall, R. L. and Marshall, V. R., 1988. A discretized population balance for nucleation, growth and aggregation. American Institute of Chemical Engineering Journal, 34: 1821-1832.

Hounslow, M. J., Bramley, A. S. and Paterson, W. R., 1998. Aggregation during precipitation from solution. A pore diffusion reaction model for calcium oxalate. Journal of Colloid and Interface Science, 203: 383-391.

Hounslow, M. J., Mumtaz, H. S., Collier, A. P., Barrick, J. P. and Bramley, A. S., 2001. A micro-mechanical model for the rate of aggregation during precipitation from solution. Chemical Engineering Science, 56: 2543-2552.

Janzel, J. G., de Souza, L. B. S. and Schultz, H. E., 2003. Kinetic energy in grid turbulence: comparison between data and theory. Journal of Brazilian Society and Mechanical Science and Engineering, 4: 347-351.

Jones, A. G., 2002. Crystallization process systems. Butterworth – Heinemann, Oxford.

Kashchiev, D., 2000. Nucleation, basic theory with application. Butterworth Heinemann, Oxford.

Kavanagh, J. P., 1992. Methods for the study of calcium oxalate crystallization and their application to urolithiases research. Scanning Microscopy, 6: 685-705.

Kramer, T. A. and Clark, M. M., 1999. Incorporation of aggregate breakup in the simulation of orthokinetic coagulation. Journal of Colloid and Interface Science, 216: 116-126

Kruis, F. E. and Kusters, K. A. 1997. The collision rate of particles in turbulent flow. Journal of Aerosol Science, 158: 201-230.

Lee, K. C. and Yianneskis, M., 1988. Turbulence properties of the impeller stream of a rushton turbine. American Institute of Chemical Engineering Journal, 44:13-24.

Lewis, A. E., Kramer, H., and Nathoo, J., 2008. Crystallization and precipitation. Cape Town: University of Cape Town (lecture notes).

Matsunga, N., Sugihara, Y., Komatsu, T. and Masuda, A., 1999. Quantitative properties of oscillating-grid turbulence in a homogeneous fluid. Fluid Dynamic Research, 25: 147-165.

Mersmann, A. and Franke, J., 1993. Thermal analysis of solids production processes. Chemical Engineering Technology, 16: 75-81.

Mersman, A. (ed.), 2001. Crystallization technology handbook. Marcel Dekker, USA.

Meyerson, A. S., 2002. Handbook of industrial crystallization. Butterworth-Heinemann, Oxford.

Militaru, R., 2001. Dimensional characterizations of homogeneous and isotropic turbulence. Computer Methods in Applied Mechanics and Engineering, 190: 2369-2376.

Mullin, J. W., 2001. Crystallization. Butterworth - Heinemann, London.

Mullin, J. W., 1972. Crystallization. Butterworth and Co, London.

Mumtaz, H. S. and Hounslow, M. J., 2000. Aggregation during precipitation from solution: an experimental investigation using Poiseuille flow. Chemical Engineering Science, 55: 5671-5681.

Mumtaz, H.S., Hounslow, M.J., and Paterson, W. R., 2000. Orthokinetic aggregation during precipitation: A computational model for calcium oxalate monohydrate., Institute of Chemical .Engineers., 75: 152-159.

Nagata, S., 1975. Mixing: Principles and applications. Wiley, New York.

Nielsen, A. E. and Toft, J. M., 1984. Electrolyte crystal growth kinetics. Journal of Crystal Growth, 67:278-288.

Orlins, J. J. and Gulliver, J. S., 2003. Turbulence quantification and sediment re- suspension in an oscillating grid chamber. Experiments in Fluids, 34: 662-677.

Paul, E. L., Atoemmo-Obeng, V. A. and Kresta, S. M. (eds), 2004. Handbook of industrial mixing: science and practice. Wiley and sons, Inc., Canada.

Randolph, A. D. and Larson, M. A., 1962. Transient and steady-state size distribution in continuous mixed-suspension crystallizers. American Institute of Chemical Engineering Journal, 85: 639-645.

Randolph, A. D. and Larson, M. A., 1988. Theory of particulate processes. Academic Press, New York.

Schafer, M., Hofken, M. and Durst, F., 1997. Detailed LDV measurements for visualization of the flow within a stirred reactor equipped with a rushton turbine. Transactions of the Institute of Chemical Engineers, 75: 729-739.

Schubert, H. and Bischofberger, C., 1998. Microprocess air dispersion and particle bubble attachment in flotation machines as well as consequences for the scale up of macroprocesses. International Journal of Mineral Processing, 52: 245-259.

Schuetz, S. and Piesche, M., 2002. A model of the coagulation process with solid particles and flocs in turbulent flow. Chemical Engineering Science, 57: 4537- 4368.

Scholtz, R., 2006. Melt crystallization in the future, actual trends and future developments. 13th International workshop on industrial crystallization BIWC, Netherlands.

Shy, S. S., Tang, C. Y. and Fann, S. Y., 1997. A nearly isotropic turbulence generated by a pair of vibrating grids. Experimental Thermal and Fluid Science, 14: 251-262.

Smith, J. M., 1990. Industrial needs for mixing research. Transactions of the Institution of Chemical Engineers, 68: 3-6.

Söhnel, O. and Garside, J., 1992. Precipitation. Basic principles and industrial application. Butterworth - Heinemann., London.

Söhnel, O., and Mullin, J. W., 1991. Aggregation in batch precipitated suspension. Particle design via crystallization. American Institute of Chemical Engineering Symposium Series, 87:182-189.

Soos, M., Moussa, A. S., Erhl, L., Sefcik, J., Wu, H. and Morbidelli, M., 2008. The effect of shear rate on aggregate size and morphology investigated under turbulent conditions in stirred tank. Journal of Colloid and Interface Science, 319: 577-589.

Srdic, A., Fernando, H. J. S. and Montenegro, L., 1996. Generation of nearly isotropic turbulence using two oscillating grids. Experiments in Fluids, 20: 297-395.

Staffman, P. G. and Turner, J. S., 1956. On collision of drops in turbulent clouds. Journal of. Fluid Mechanics, 1: 16-30.

Stumm, W. and Morgan, J. J., 1981. Aquatic chemistry: an introduction emphasizing chemical equilibrium in natural waters. John Wiley and sons, New York.

Thompson, S. M. and Turner, J. S., 1975. Mixing across an interface due to turbulence generated by an oscillating grid. Journal of Fluid mechanics, 67: 349-368.

Thongboonkerd, V., Semangoen, T. and Chutipongatanate, S., 2006. Factors determining types and morphologies of calcium oxalate crystals: Molar concentrations, buffering, pH, stirring and temperature. Clinica Chimica Acta, 367: 120-131.

Vicum, L., Ottiger, S., Mazzotti, M., Makowski, L. and Baldyga, J., 2004. Multi-scale modelling of a reactive mixing process in a semi-batch stirred tank. Chemical Engineering Science, 59: 1767-1781.

Zauner, R. and Jones, A. G., 2000. Determination of nucleation, growth, agglomeration and disruption kinetics from experimental precipitation data: the calcium oxalate system. Chemical Engineering Science, 55: 4219-4232.

Zauner, R. and Jones, A. G., 2000. On the influence of mixing on crystal precipitation processes-application of the segregated feed model. Chemical Engineering Science, 57: 821-831.

Appendices

Appendix A: Oscillating grid characterisation

Sample calculations used in this study to characterise the oscillating grid crystallizer operating parameters are shown below.

Constants

n_g: 19

A_c: 0.0227m^2

C_p: 97

d: 0.001m

m_L: 9.95kg

S: 0.018m

v: 8.9x$10^{-7}$$m^2.s^{-1}$

ρ: 1000$kg.m^{-3}$

σ: 0.22

Grids reynolds number

$$R_N = \frac{fSd}{v}$$

Power inputs of the grids

$$P_g = C_p \rho A_c \sigma f^3 S^3 R_N^{-\sigma}$$

Rate of energy dissipation per unit mass

$$\varepsilon = \frac{n_g P_g}{m_L}$$

Appendix B: Particle size distribution

Particle size distribution was measured using a Malvern Mastersizer-S instrument supplied by Malvern Instruments. The instrument gives the result as a volume distribution (Table A-1) and this had to be converted into a number distribution (Table A-2) on an excel spreadsheet. The conversion is illustrated below as well as the calculation of moments from the distribution.

Table A-1 volume based distribution

Size (µm)	Volume In %	Size (µm)	Volume In %	Size (µm)	Volume In %	Size (µm)	Volume In %	Size (µm)	Volume In %	Size (µm)	Volume In %
0.010	0.00	0.080	0.00	0.634	0.00	5.053	2.06	40.244	0.83	320.535	0.00
0.011	0.00	0.090	0.00	0.717	0.02	5.709	2.70	45.469	0.03	362.148	0.00
0.013	0.00	0.102	0.00	0.810	0.06	6.450	3.47	51.371	0.00	409.163	0.00
0.014	0.00	0.115	0.00	0.915	0.08	7.287	4.36	58.041	0.00	462.281	0.00
0.016	0.00	0.130	0.00	1.034	0.10	8.233	5.32	65.575	0.00	522.296	0.00
0.018	0.00	0.147	0.00	1.168	0.12	9.302	6.28	74.089	0.00	590.102	0.00
0.021	0.00	0.166	0.00	1.320	0.14	10.510	7.17	83.707	0.00	666.711	0.00
0.024	0.00	0.187	0.00	1.491	0.18	11.874	7.88	94.574	0.00	753.265	0.00
0.027	0.00	0.211	0.00	1.684	0.24	13.416	8.31	106.852	0.00	851.056	0.00
0.030	0.00	0.239	0.00	1.903	0.31	15.157	8.40	120.724	0.00	961.542	0.00
0.034	0.00	0.270	0.00	2.150	0.38	17.125	8.11	136.397	0.00	1086.372	0.00
0.038	0.00	0.305	0.00	2.429	0.47	19.348	7.46	154.104	0.00	1227.408	0.00
0.043	0.00	0.345	0.00	2.745	0.57	21.860	6.49	174.110	0.00	1386.753	0.00
0.049	0.00	0.389	0.00	3.101	0.71	24.698	5.32	196.714	0.00	1566.785	0.00
0.055	0.00	0.440	0.00	3.503	0.90	27.904	4.08	222.251	0.00	1770.189	0.00
0.062	0.00	0.497	0.00	3.958	1.18	31.527	2.88	251.105	0.00	2000.000	
0.070	0.00	0.561	0.00	4.472	1.56	35.620	1.84	283.704	0.00		
0.080		0.634		5.053		40.244		320.535			

Table A-2 Number based distribution

			N (#.m^{-3})					
sizes (μm)	ΔL (m)	Lbar (m)	10 mins	20 mins	30 mins	40 mins	50 mins	60 mins
0.01								
0.011298	1.298E-09	1.1947E-08	0.000E+00	0.000E+00	0.000E+00	0.000E+00	0.000E+00	0.000E+00
0.012765	1.467E-09	1.34985E-08	0.000E+00	0.000E+00	0.000E+00	0.000E+00	0.000E+00	0.000E+00
0.014422	1.657E-09	1.52505E-08	0.000E+00	0.000E+00	0.000E+00	0.000E+00	0.000E+00	0.000E+00
0.016295	1.873E-09	1.72315E-08	0.000E+00	0.000E+00	0.000E+00	0.000E+00	0.000E+00	0.000E+00
0.01841	2.115E-09	1.94675E-08	0.000E+00	0.000E+00	0.000E+00	0.000E+00	0.000E+00	0.000E+00
0.0208	2.39E-09	2.1995E-08	0.000E+00	0.000E+00	0.000E+00	0.000E+00	0.000E+00	0.000E+00
0.0235	2.7E-09	2.485E-08	0.000E+00	0.000E+00	0.000E+00	0.000E+00	0.000E+00	0.000E+00
0.026551	3.051E-09	2.80765E-08	0.000E+00	0.000E+00	0.000E+00	0.000E+00	0.000E+00	0.000E+00
0.029998	3.447E-09	3.17215E-08	0.000E+00	0.000E+00	0.000E+00	0.000E+00	0.000E+00	0.000E+00
0.033892	3.894E-09	3.5839E-08	0.000E+00	0.000E+00	0.000E+00	0.000E+00	0.000E+00	0.000E+00
0.038292	4.4E-09	4.0492E-08	0.000E+00	0.000E+00	0.000E+00	0.000E+00	0.000E+00	0.000E+00
0.043264	4.972E-09	4.575E-08	0.000E+00	0.000E+00	0.000E+00	0.000E+00	0.000E+00	0.000E+00
0.04888	5.616E-09	5.1688E-08	0.000E+00	0.000E+00	0.000E+00	0.000E+00	0.000E+00	0.000E+00
0.055226	6.346E-09	5.8399E-08	0.000E+00	0.000E+00	0.000E+00	0.000E+00	0.000E+00	0.000E+00
0.062396	7.17E-09	6.5981E-08	0.000E+00	0.000E+00	0.000E+00	0.000E+00	0.000E+00	0.000E+00
0.070496	8.1E-09	7.4546E-08	0.000E+00	0.000E+00	0.000E+00	0.000E+00	0.000E+00	0.000E+00
0.079648	9.152E-09	8.4224E-08	0.000E+00	0.000E+00	0.000E+00	0.000E+00	0.000E+00	0.000E+00
0.089988	1.034E-08	9.5158E-08	0.000E+00	0.000E+00	0.000E+00	0.000E+00	0.000E+00	0.000E+00
0.101671	1.1683E-08	1.07513E-07	0.000E+00	0.000E+00	0.000E+00	0.000E+00	0.000E+00	0.000E+00
0.11487	1.3199E-08	1.2147E-07	0.000E+00	0.000E+00	0.000E+00	0.000E+00	0.000E+00	0.000E+00

			N (#.m^{-3})					
sizes (μm)	ΔL (m)	Lbar (m)	10 mins	20 mins	30 mins	40 mins	50 mins	60 mins
0.129783	1.4913E-08	1.3724E-07	0.000E+00	0.000E+00	0.000E+00	0.000E+00	0.000E+00	0.000E+00
0.146631	1.6848E-08	1.55055E-07	0.000E+00	0.000E+00	0.000E+00	0.000E+00	0.000E+00	0.000E+00
0.165667	1.9036E-08	1.75185E-07	0.000E+00	0.000E+00	0.000E+00	0.000E+00	0.000E+00	0.000E+00
0.187175	2.1508E-08	1.97929E-07	0.000E+00	0.000E+00	0.000E+00	0.000E+00	0.000E+00	0.000E+00
0.211474	2.4299E-08	2.23624E-07	0.000E+00	0.000E+00	0.000E+00	0.000E+00	0.000E+00	0.000E+00
0.238928	2.7454E-08	2.52655E-07	0.000E+00	0.000E+00	0.000E+00	0.000E+00	0.000E+00	0.000E+00
0.269947	3.1019E-08	2.85457E-07	0.000E+00	0.000E+00	0.000E+00	0.000E+00	0.000E+00	0.000E+00
0.304992	3.5045E-08	3.22515E-07	0.000E+00	0.000E+00	0.000E+00	0.000E+00	0.000E+00	0.000E+00
0.344587	3.9595E-08	3.64385E-07	0.000E+00	0.000E+00	0.000E+00	0.000E+00	0.000E+00	0.000E+00
0.389322	4.4735E-08	4.1169E-07	0.000E+00	0.000E+00	0.000E+00	0.000E+00	0.000E+00	0.000E+00
0.439865	5.0543E-08	4.65137E-07	0.000E+00	0.000E+00	0.000E+00	0.000E+00	0.000E+00	0.000E+00
0.496969	5.7104E-08	5.25521E-07	0.000E+00	0.000E+00	0.000E+00	0.000E+00	0.000E+00	0.000E+00
0.561487	6.4518E-08	5.93746E-07	0.000E+00	0.000E+00	0.000E+00	0.000E+00	0.000E+00	0.000E+00
0.634381	7.2894E-08	6.70828E-07	0.000E+00	0.000E+00	0.000E+00	0.000E+00	0.000E+00	0.000E+00
0.716738	8.2357E-08	7.57917E-07	0.000E+00	0.000E+00	0.000E+00	0.000E+00	0.000E+00	0.000E+00
0.809787	9.3049E-08	8.56312E-07	0.000E+00	0.000E+00	0.000E+00	0.000E+00	0.000E+00	0.000E+00
0.914916	1.05129E-07	9.67481E-07	2.783E+09	3.552E+09	2.625E+09	2.701E+09	3.021E+09	2.774E+09
1.033693	1.18777E-07	1.09308E-06	7.384E+09	9.348E+09	6.483E+09	5.646E+09	6.303E+09	5.808E+09
1.167889	1.34196E-07	1.23499E-06	7.146E+09	8.974E+09	5.831E+09	5.586E+09	6.188E+09	5.786E+09
1.319508	1.51619E-07	1.39532E-06	5.873E+09	7.349E+09	4.636E+09	4.374E+09	4.842E+09	4.549E+09
1.49081	1.71302E-07	1.57646E-06	4.713E+09	5.854E+09	3.573E+09	3.347E+09	3.696E+09	3.480E+09

			N (#.m^{-3})					
sizes (μm)	ΔL (m)	Lbar (m)	10 mins	20 mins	30 mins	40 mins	50 mins	60 mins
1.684351	1.93541E-07	1.78112E-06	3.986E+09	4.892E+09	2.894E+09	2.679E+09	2.938E+09	2.767E+09
1.903018	2.18667E-07	2.01235E-06	3.572E+09	4.321E+09	2.481E+09	2.252E+09	2.444E+09	2.298E+09
2.150073	2.47055E-07	2.2736E-06	3.261E+09	3.891E+09	2.188E+09	1.950E+09	2.089E+09	1.965E+09
2.429201	2.79128E-07	2.56877E-06	2.915E+09	3.440E+09	1.906E+09	1.677E+09	1.771E+09	1.671E+09
2.744567	3.15366E-07	2.90225E-06	2.515E+09	2.942E+09	1.615E+09	1.413E+09	1.471E+09	1.398E+09
3.100874	3.56307E-07	3.27903E-06	2.119E+09	2.466E+09	1.348E+09	1.184E+09	1.216E+09	1.170E+09
3.503438	4.02564E-07	3.70472E-06	1.787E+09	2.078E+09	1.139E+09	1.012E+09	1.029E+09	1.005E+09
3.958263	4.54825E-07	4.18568E-06	1.538E+09	1.795E+09	9.979E+08	8.978E+08	9.087E+08	8.987E+08
4.472136	5.13873E-07	4.72907E-06	1.361E+09	1.599E+09	9.098E+08	8.246E+08	8.367E+08	8.345E+08
5.052721	5.80585E-07	5.34301E-06	1.233E+09	1.460E+09	8.555E+08	7.746E+08	7.917E+08	7.919E+08
5.708679	6.55958E-07	6.03666E-06	1.131E+09	1.350E+09	8.156E+08	7.317E+08	7.552E+08	7.542E+08
6.449795	7.41116E-07	6.82035E-06	1.038E+09	1.247E+09	7.766E+08	6.859E+08	7.151E+08	7.110E+08
7.287125	8.3733E-07	7.70579E-06	9.422E+08	1.139E+09	7.286E+08	6.308E+08	6.639E+08	6.561E+08
8.233159	9.46034E-07	8.70618E-06	8.406E+08	1.019E+09	6.689E+08	5.659E+08	6.006E+08	5.893E+08
9.30201	1.06885E-06	9.83644E-06	7.320E+08	8.894E+08	5.968E+08	4.926E+08	5.265E+08	5.128E+08
10.509622	1.20761E-06	1.11134E-05	6.194E+08	7.532E+08	5.158E+08	4.148E+08	4.460E+08	4.311E+08
11.87401	1.36439E-06	1.25562E-05	5.076E+08	6.172E+08	4.306E+08	3.371E+08	3.642E+08	3.495E+08
13.415526	1.54152E-06	1.41863E-05	4.017E+08	4.881E+08	3.465E+08	2.640E+08	2.862E+08	2.726E+08
15.157166	1.74164E-06	1.6028E-05	3.059E+08	3.711E+08	2.678E+08	1.984E+08	2.157E+08	2.039E+08
17.12491	1.96774E-06	1.81088E-05	2.238E+08	2.709E+08	1.985E+08	1.430E+08	1.556E+08	1.461E+08
19.348112	2.2232E-06	2.04597E-05	1.568E+08	1.894E+08	1.409E+08	9.850E+07	1.073E+08	1.000E+08
21.859937	2.51183E-06	2.31158E-05	1.050E+08	1.264E+08	9.538E+07	6.470E+07	7.041E+07	6.519E+07

`			N (#.m^{-3})					
sizes (μm)	ΔL (m)	Lbar (m)	10 mins	20 mins	30 mins	40 mins	50 mins	60 mins
24.697853	2.83792E-06	2.61168E-05	6.695E+07	8.030E+07	6.144E+07	4.036E+07	4.382E+07	4.027E+07
27.904195	3.20634E-06	2.95074E-05	4.040E+07	4.823E+07	3.743E+07	2.374E+07	2.567E+07	2.341E+07
31.526793	3.6226E-06	3.33381E-05	2.298E+07	2.727E+07	2.148E+07	1.311E+07	1.408E+07	1.272E+07
35.619687	4.09289E-06	3.76661E-05	1.222E+07	1.438E+07	1.153E+07	6.715E+06	7.142E+06	6.368E+06
40.243931	4.62424E-06	4.25561E-05	5.970E+06	6.934E+06	5.675E+06	3.118E+06	3.268E+06	2.861E+06
45.468507	5.22458E-06	4.80808E-05	2.653E+06	3.027E+06	2.572E+06	1.211E+06	1.209E+06	9.934E+05
51.371352	5.90285E-06	5.43228E-05	8.326E+05	8.841E+05	7.935E+05	2.693E+05	2.321E+05	1.492E+05
58.04052	6.66917E-06	6.13751E-05	2.225E+04	0.000E+00	0.000E+00	0.000E+00	0.000E+00	0.000E+00

The excel formulae used to perform the conversion of the volume distribution to number distribution are shown below:

$$\Delta L = \left(\frac{94.57 - 83.71}{1000000} \right) = 1.09\,E - 05$$

$$Lbar = \left(\frac{94.57}{1000000} \right) + \frac{\Delta L}{2}$$

$$N = \left(\frac{vol\%}{100} \right) x \frac{V}{\left(\frac{\Pi}{6} x Lbar^3 \right)}$$

Where V is the volume of the solids and N is the number distribution.

m0 = sum(N)

m1 = sum(lbar x N)

m2 = sum($lbar^2$ x N)

m3 = sum($lbar^3$ x N

m4 = sum($lbar^4$ x N)

m_0 is the zeroth moment.....m_4 = fourth moment

Appendix C: Repeatability of particle size distribution

The particle size distribution experiments were done in triplicate. The results presented in Table B-1 are the individual runs measurements for time 10 – 60 mins. It was found that the trends in particle size distribution were reproducible but not the actual numbers (m_0) of particles. The result presented below were use to illustrate the repeatability of the distribution. These are results for an experiments carried out at 0 - 0.41 W/kg.

Table B-1 A Variation of $L_{1,0}$ for repeatability experiments

10 mins [Lbar]			
ε (W/ kg)	run1	run2	run3
0	3.26348E-06	3.27522E-06	3.27242E-06
0.049	2.78367E-06	2.88232E-06	2.93444E-06
0.1	2.66325E-06	2.74154E-06	2.79531E-06
0.25	2.64662E-06	2.72527E-06	2.77588E-06
0.41	3.26045E-06	2.91808E-06	3.3153E-06

20 mins [Lbar]			
ε (W/ kg)	run1	run2	run3
0	3.26348E-06	3.47311E-06	3.4694E-06
0.049	2.65472E-06	2.7318E-06	2.78025E-06
0.1	2.62979E-06	2.69262E-06	2.73984E-06
0.25	2.60565E-06	2.66072E-06	2.70285E-06
0.41	3.29549E-06	3.31113E-06	3.32791E-06

30 mins [Lbar]			
ε (W/ kg)	run1	run2	run3
0	3.51831E-06	3.5149E-06	3.51174E-06
0.049	2.14206E-06	2.18804E-06	2.21884E-06
0.1	2.66578E-06	2.72142E-06	2.77018E-06
0.25	2.53289E-06	2.56568E-06	2.5903E-06
0.41	3.01011E-06	3.82754E-06	3.83089E-06

40 mins [Lbar]			
ε (W/ kg)	run1	run2	run3
0	3.52663E-06	3.5165E-06	3.5127E-06
0.049	2.57137E-06	2.63729E-06	2.67769E-06
0.1	2.52111E-06	2.23442E-06	2.26085E-06
0.25	2.51534E-06	2.5406E-06	2.57051E-06
0.41	3.15936E-06	3.15745E-06	3.15976E-06

50 mins [Lbar]			
ε (W/ kg)	run1	run2	run3
0	4.1521E-06	4.15771E-06	4.01781E-06
0.049	2.54257E-06	2.60305E-06	2.6438E-06
0.1	2.48449E-06	2.526E-06	2.55557E-06
0.25	2.48057E-06	2.50148E-06	2.5156E-06
0.41	3.1158E-06	3.11887E-06	3.12076E-06

60mins [Lbar]			
ε (W/ kg)	run1	run2	run3
0	4.04245E-06	4.04911E-06	4.05729E-06
0.049	2.50429E-06	2.55101E-06	2.59313E-06
0.1	2.51614E-06	2.54629E-06	2.57764E-06
0.25	2.52912E-06	2.54863E-06	2.5639E-06
0.41	3.06924E-06	3.07641E-06	3.0853E-06

Table B-2 A Variation of $D_{4,3}$ for repeatability experiments

10 mins [d4,3]			
ε (W/ kg)	run1	run2	run3
0	1.50662E-05	1.47976E-05	1.46165E-05
0.049	1.72742E-05	1.62913E-05	1.57846E-05
0.1	1.76121E-05	1.67816E-05	1.61911E-05
0.25	1.75309E-05	1.68219E-05	1.63679E-05
0.41	1.61367E-05	1.40821E-05	1.56246E-05

20 mins [d4,3]			
ε (W/ kg)	run1	run2	run3
0	1.49252E-05	1.47451E-05	1.45798E-05
0.049	1.75707E-05	1.66234E-05	1.61191E-05
0.1	1.74896E-05	1.68064E-05	1.63457E-05
0.25	1.73733E-05	1.67334E-05	1.63227E-05
0.41	1.66809E-05	1.63511E-05	1.61608E-05

30 mins [d,43]			
ε (W/ kg)	run1	run2	run3
0	1.45308E-05	1.4379E-05	1.41091E-05
0.049	1.71477E-05	1.65204E-05	1.61566E-05
0.1	1.8255E-05	1.75677E-05	1.70285E-05
0.25	1.70806E-05	1.67112E-05	1.64452E-05
0.41	1.57871E-05	1.5378E-05	1.52835E-05

40 mins [Lbar]			
ε (W/ kg)	run1	run2	run3
0	1.38873E-05	1.38317E-05	1.37381E-05
0.049	1.74065E-05	1.66504E-05	1.6193E-05
0.1	1.6907E-05	1.70454E-05	1.64534E-05
0.25	1.69789E-05	1.66453E-05	1.63613E-05
0.41	1.63353E-05	1.62222E-05	1.61199E-05

50 mins [d 4,3]			
ε (W/ kg)	run1	run2	run3
0	1.25472E-05	1.24616E-05	1.20942E-05
0.049	1.72497E-05	1.6587E-05	1.61747E-05
0.1	1.68924E-05	1.649E-05	1.61798E-05
0.25	1.67664E-05	1.6501E-05	1.62924E-05
0.41	1.6156E-05	1.60674E-05	1.59521E-05

60mins [d4,3]			
ε (W/ kg)	run1	run2	run3
0	1.26506E-05	1.25906E-05	1.25717E-05
0.049	1.72032E-05	1.65755E-05	1.61883E-05
0.1	1.6579E-05	1.61993E-05	1.59585E-05
0.25	1.5976E-05	1.58332E-05	1.5702E-05
0.41	1.60966E-05	1.60326E-05	1.59918E-05

Appendix D: X-ray diffraction patterns

The X-ray diffraction patterns for different energy inputs are shown below.

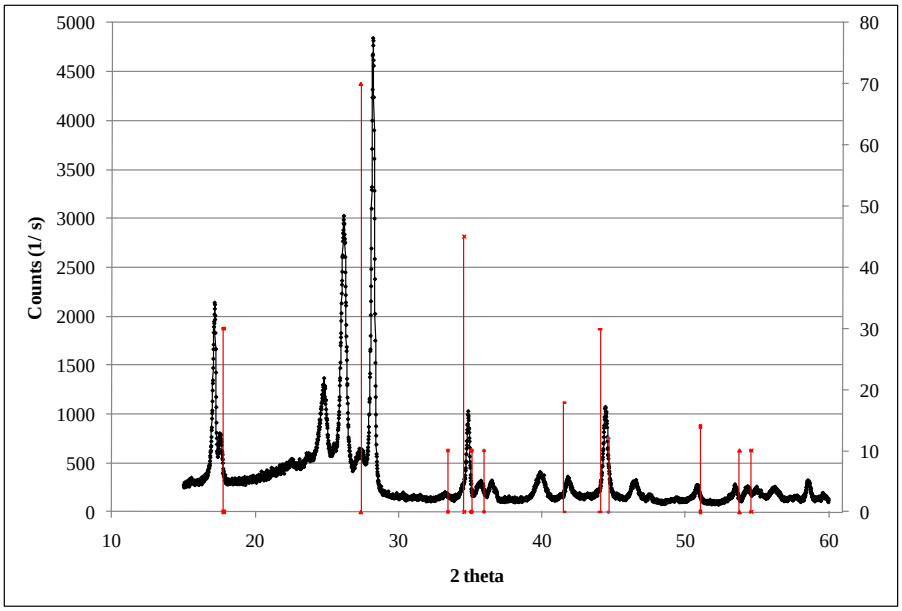

Figure C-1 XRD graph with reference pattern for 0 W/ kg

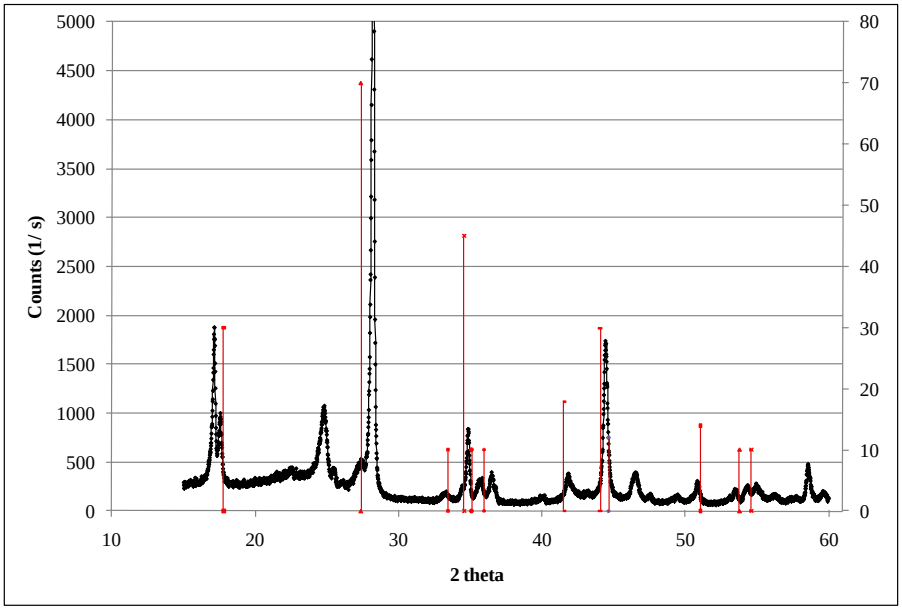

Figure C-2 XRD graph with reference pattern for 0.1 W/ kg

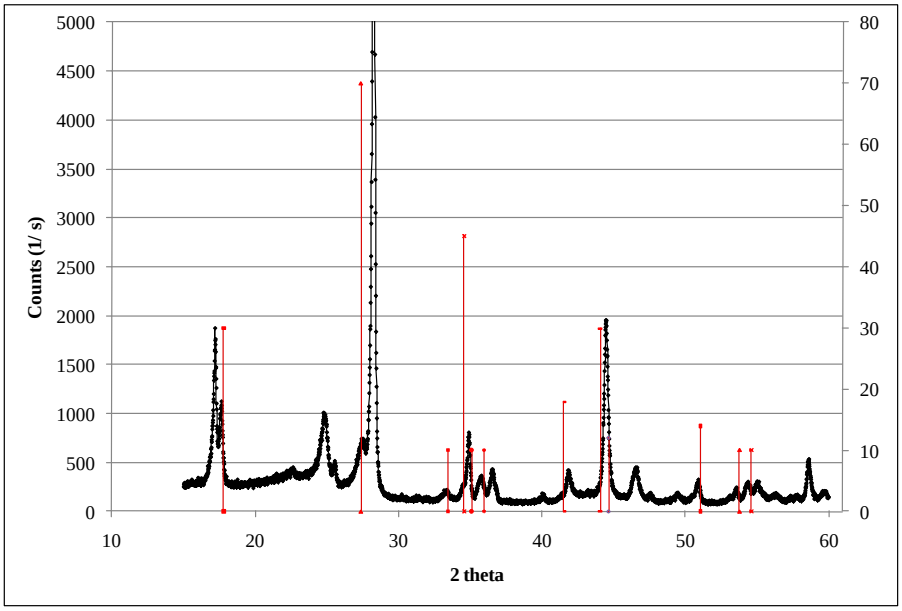

Figure C-3 XRD graph with reference pattern for 0.25 W/ kg

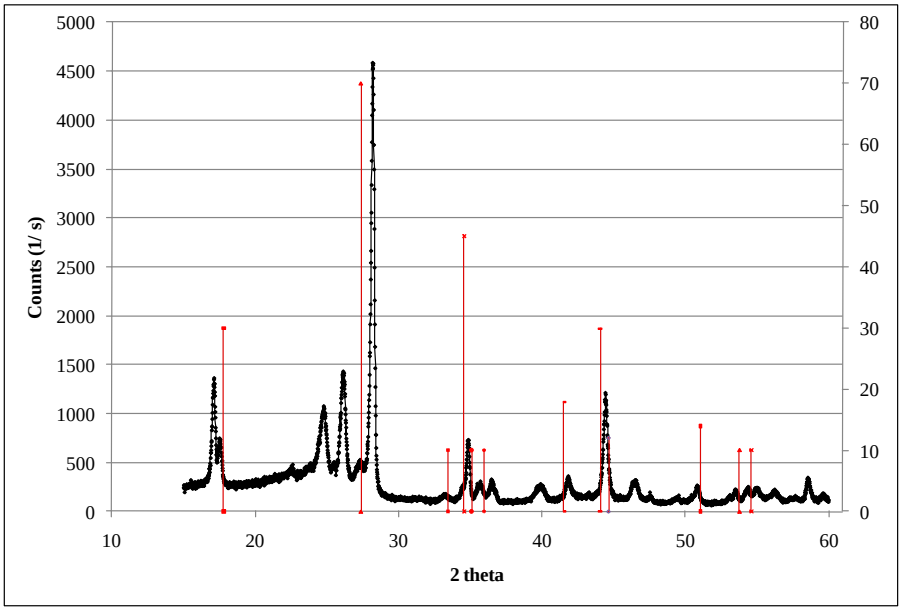

Figure C-4 XRD graph with reference pattern for 0.41 W/ kg